# Estimating Coherent Contributions to the Error Profile Using Cycle Error Reconstruction

Arnaud Carignan-Dugas<sup>1</sup>, Shashank Kumar Ranu<sup>2,3</sup>, and Patrick Dreher<sup>4,5</sup>

Mitigation and calibration schemes are central to maximize the computational reach of today's Noisy Intermediate Scale Quantum (NISQ) hardware, but these schemes are often specialized to exclusively address either coherent or decoherent error sources. Quantifying the two types of errors hence constitutes a desirable feature when it comes to benchmarking error suppression tools. In this paper, we present a scalable and cycle-centric methodology for obtaining a detailed estimate of the coherent contribution to the error profile of a computing cycle. The protocol that we suggest is based on Cycle Error Reconstruction (CER), also known as K-body Noise Reconstruction (KNR). This protocol is similar to Cycle Benchmarking (CB) in that it provides a cycle-centric diagnostic based on Pauli fidelity estimation [1]. We introduce an additional hyper-parameter in CER by allowing the hard cycles to be folded multiple times before being subject to Pauli twirling. Performing CER for different values of our added hyper-parameter allows estimating the coherent error contributions through a generalization of the fidelity decay formula. We confirm the accuracy of our method through numerical simulations on a quantum simulator, and perform proof-of-concept experiments on three IBM chips, namely ibmq guadalupe, ibmq manila, and ibmq montreal. In all three experiments, we measure substantial coherent errors biased in Z.

Patrick Dreher: Corresponding author: padreher@ncsu.edu

<sup>&</sup>lt;sup>1</sup> Keysight Technologies Canada, Kanata, ON K2K 2W5, Canada

<sup>&</sup>lt;sup>2</sup> Department of Electrical Engineering, Indian Institute of Technology Madras, Chennai 600036, India

<sup>&</sup>lt;sup>3</sup> Department of Physics, Indian Institute of Technology Madras, Chennai 600036, India

<sup>&</sup>lt;sup>4</sup> Department of Electrical and Computer Engineering, North Carolina State University, Raleigh, NC 27695, USA

<sup>&</sup>lt;sup>5</sup> Department of Physics, North Carolina State University, Raleigh, NC 27695, USA

#### 1 Introduction

Today's engineering advances in quantum computing hardware architectures allow vendors to produce processors with a considerable number of qubits. Despite these impressive advances, the current technology does not yet enable large-scale fault-tolerant quantum computing (FTQC) to be implemented. As a result, computations today and into the intermediate future will be done on Noisy Intermediate-Scale Quantum (NISQ) [2] platforms. Noise on these devices can result in both decoherent and coherent errors. Suppressing noise on these hardware platforms and extending the coherence times will rely on improvements in error mitigation protocols and error suppression methods.

Decoherent errors are created by the unwanted interactions between the qubits and their external environment as well as by stochastic events. Typical decoherent processes include amplitude-damping, phase-damping, and depolarization. Decoherent errors are often partially suppressed by dynamical decoupling (DD) techniques [3–12]. Moreover, many error mitigation schemes rely on the propagation laws of decoherent errors to suppress their effect on computational outcomes [13–30].

Coherent errors are the result of unitary processes occurring in the closed system formed by the qubits' Hilbert space. They arise from several sources such as miscalibrated control parameters, external fields, and crosstalk (e.g. undesired internal fields). They are usually suppressed through advanced calibration and pulse compensation methods [31–34]. Alternatively, coherent errors can be effectively transformed into decoherent errors via Randomized Compiling (RC) [35, 36], and then mitigated with tools aimed for decoherent errors [30].

Because the two types of errors have different natures, there are specific error suppression tools aim at suppressing only coherent errors, while others impact decoherent errors either exclusively, or more efficiently. Given the fundamentally different nature of coherent and decoherent errors and the likelihood that FTQC will not be available in the intermediate future, it will be important to develop fast and accurate methods to independently measure their impact on quantum computing outcomes. Developing such capabilities can provide an essential means to test and compare the effect of different error suppression and calibration tools.

There exist many different frameworks and protocols for characterizing quantum computing processing errors. One approach focuses on characterizing specific infinitesimal generators of motion from a Hamiltonian or Lindbladian viewpoint. While crucial, such approaches don't immediately connect with the diagnostics of integrated evolutions such as quantum gates. Let's define a quantum instruction as a set of one or few qudit labels, together with a linear operation to apply over these. The operation can be a gate, some measurement operation, or some state preparation. A cycle can be defined as a set of instructions targeting disjoint sets of qubits, together with a schedule. For example, a cycle could consist of a round of simultaneous CNOT gates over the processor. Due to various physical effects such as crosstalk, parallel instructions often substantially influence each other. This observation means that characterizing instructions in isolation can lead to misguided diagnostics. Indeed, a cycle error channel

depends on a non-obvious function of every instruction that is being applied, as well as on the precise relative timing of those instructions.

As such, to better contextualize error profiles, we focus on a cycle-centric approach to process characterization. Given the considerable number of parallelizable instructions as well as the complexity of their joint error profile, a cycle-centric approach is particularly relevant in the NISQ-era and beyond. A well-known cycle-centric error diagnostic scheme is known as Gate Set Tomography (GST) [37–42]. GST provides detailed information about both coherent and decoherent errors, but the diagnostic information addresses non-randomized cycles. In the current work, we instead focus on characterizing effective dressed cycles tied to randomly compiled circuits. The idea is to provide detailed diagnostic information that closely connects with the effective performance of circuits run under RC.

One convenient aspect of effective dressed cycles is that they can be characterized via Pauli infidelity estimation methods [43, 44]. In particular, the Cycle Benchmarking (CB) [1] protocol features a valuable framework to characterize effective dressed cycles with great precision. As such, more advanced error diagnostic tools, such as Cycle Error Reconstruction (CER) [34, 45], repurposed the structure of CB circuits to gather detailed error profiles attached to effective dressed cycles. Note that CER is also known as k-body Noise Reconstruction (KNR) [46].

However, neither CB nor CER are designed to provide a budget for coherent and decoherent contributions to the measured error rates. We introduce a new CB-structured method for separately measuring both the decoherent and coherent cycle errors based on CER data. To distinguish between decoherent and coherent errors, we rely on their different propagation principles (linear vs quadratic).

In this paper we layout our work as follows. In Section 2, we summarize the main principles describing the propagation of coherent and decoherent errors in repeated error channels. In Section 3, we outline the background material necessary to understand a CB-structured error characterization scheme known as CER [34, 45], and we introduce our protocol extension to CER. We finish the section with a generalized decay model that connects the output data of the scheme to the effective coherent contributions to the error profile. In Section 4, we further expand on the fitting model related to our protocol. This section also provides numerical evidence that the error profile obtained from our suggested experiment matches the underlying error model. In Section 5, we apply our extension to the CER protocol on three separate IBM quantum computing hardware platforms and present the central results of this research. As a proof of concept, we measure the effective coherent and decoherent error rates marginalized on an ancilla during an entangling cycle. Fidelities of the errors for various sequence lengths are calculated and compared to the results obtained from running the circuit applying a proposed polynomial global fitting function. We show through our implementations that the coherent error manifests primarily as Pauli Z error on IBM platforms due to ZZ static coupling in transmon qubits. In Section 6, we summarize our results and expand on their relevance regarding the benchmarking and designing of error suppression tools for gate-based quantum computing architectures. In addition, there are several

supplemental sections that expand the discussion in the main sections of the paper.

# 2 Theory - Coherent and decoherent error propagation

Coherent and decoherent quantum errors in a quantum computing circuit propagate in intrinsically different ways. In this section, we explicitly demonstrate the error propagation formula for the simple case of an x-fold error channel  $\mathcal{E}^x$ .

Recent work has also analyzed the error propagation in quantum computers [47]. They have shown that the decoherent error increases linearly with circuit depth but plateaus after some threshold circuit depth. Our work takes such an analysis into coherent error domain, and shows, both theoretically as well as through implementations on IBM quantum processor, that repeated coherent error propagates quadratically on the first order.

A quantum state can be described by a density matrix  $\rho$ , which is a positive semidefinite, unit-trace matrix. This allows representing pure states (if and only if the rank of  $\rho$  is 1) and a probabilistic mixture thereof. The evolution of a quantum mechanical state  $\rho$  is often described by the Schrodinger equation,

$$\frac{d}{dt}\rho = -i[H, \rho] , \qquad (1)$$

where H is a Hermitian matrix referred to as the Hamiltonian. However, the Schrodinger equation only applies to the deterministic evolution of a closed system.

For open quantum systems, a more general evolution formula is given by the Lindblad master equation [48]:

$$\frac{d}{dt}\rho = \Lambda[\rho]$$

$$:= -i[H, \rho] + \sum_{j} \left( L_{j}\rho L_{j}^{\dagger} - \frac{1}{2} (L_{j}^{\dagger}L_{j}\rho + \rho L_{j}^{\dagger}L_{j}) \right) , \qquad (2)$$

where  $L_i$  are traceless matrices referred to as Lindblad operators or Lindblad jumps, and where the linear operator  $\Lambda$  is referred to as the Lindbladian. A Lindbladian is one of the general forms of Markovian and time-homogeneous master equations describing the general non-unitary evolution of the density matrix  $\rho$ .

An error channel  $\mathcal{E}$  can be represented as a linear operator acting on density matrices. In this work, we consider error channels  $\mathcal{E}$  which are close to the identity and that are the result of a finite-time evolution of a time-independent Lindbladian:

$$\mathcal{E}[\rho] = \int_{t=0}^{t=\Delta t} \Lambda[\rho] dt \ . \tag{3}$$

For what follows, we pick  $\Delta t = 1$  without loss of generality, as it simply fixes the scales of the matrices H and  $\{L_i\}_i$  appearing in the Lindbladian. We emphasize that although the  $d \times d$  matrices  $(d = 2^n)$  where n is the number of qubits H and  $L_j$  appearing in

Eq. (2) do not depend on time, we don't have to assume that the error channel  $\mathcal{E}$  is the result of a time-independent error process. The error process itself could involve time-dependent features, but could be equivalent to an integral over a time-independent evolution. Indeed, if the error process is weak (which implies that the generators of motions can be time-averaged) then after the time-dependent equation is integrated, the solution can be either exactly expressed or well approximated as the integral of a time-independent process.

Starting from Eq. (3) we can construct a columned-vectorized picture (i.e. the  $d \times d$  density matrix  $\rho$  becomes a  $d^2 \times 1$  vector  $\operatorname{col}(\rho)$  obtained by stacking the columns of  $\rho$ ) and re-write the equation as

$$\frac{d}{dt}\operatorname{col}(\rho) = \Lambda \operatorname{col}(\rho) , \qquad (4)$$

where the  $d^2 \times d^2$  matrix

$$\Lambda := -i(H \otimes \mathbb{I} - \mathbb{I} \otimes H) + \sum_{j} \left[ L_{j}^{*} \otimes L_{j} - \frac{1}{2} \left( \mathbb{I} \otimes L_{j}^{\dagger} L_{j} + L_{j}^{T} L_{j}^{*} \otimes \mathbb{I} \right) \right]$$
 (5)

is the matrix form of the Lindbladian. The solution of Eq. (4) is given by Eq. (6).

$$\operatorname{col}(\rho(t + \Delta t)) = e^{\Lambda \Delta t} \operatorname{col}(\rho(t)) \tag{6}$$

Therefore our error channel  $\mathcal{E}$  can be expressed as

$$\mathcal{E} = e^{\Lambda} \ . \tag{7}$$

In this context we are viewing  $\Lambda$  as the generator of the process matrix  $\mathcal{E}$ . Viewing  $\Lambda$  from this perspective, if all of the terms in  $\Lambda$  can be calculated, then effectively one knows the error process matrix  $\mathcal{E}$ .

To properly discuss about the strength of specific terms appearing in the Lindbladian, let's fix an expansion basis and express the effective Hamiltonian H and Lindblad operators  $L_j$  as linear combinations Pauli operators:

$$H =: \sum_{P \in \mathbb{P}_n} h_P P , \qquad (8a)$$

$$L_j =: \sum_{P \in \mathbb{P}_n} \ell_{j,P} P , \qquad (8b)$$

where  $\mathbb{P}_n$  denotes the *n*-qubit Pauli group, and where  $h_P \in \mathbb{R}$ ,  $\ell_{j,P} \in \mathbb{C}$ . In practice, the squared magnitudes  $|h_P|^2$  and  $|\ell_{j,P}|^2$  are upper-bounded by the 2-qubit error rates because they are ultimately tied to geometric near-local interactions.

In this work, we only consider errors induced by near-local physical interactions. To provide a notion of locality, we have to consider the geometric features of a given device, which in our case will simply be given by an interaction graph, where vertices are connected if qubits can undergo entangling operations. Given a connectivity graph, we

constrain Lindblad and Hamiltonian operators to be at most geometrically k-local for some small integer k, which means that the operators can act on connected subgraphs of at most k qubits (note that the operators can act trivially on some of the qubits, allowing for gaps). The accuracy of the upcoming Eq. (10) fails exponentially fast in the size of the locality constraint k. However, given some array-like topology, if we assume that errors stem from 1 or 2-body interactions in some rotating frame, then an N-qubit subsystem ( $N \leq n$ ) should be affected by O(N) terms in the Lindbladian. As a result (see Appendix A.1), the action of the error channel  $e^{\Lambda}$  on a limited qubit support can be well approximated through an early-truncated Taylor expansion.

To be more specific, first consider *Pauli fidelities*, defined for a generic channel  $\mathcal{E}$  acting on a n-qubit system as

$$f_P(\mathcal{E}) := \frac{\operatorname{Tr} P\mathcal{E}[P]}{2^n} \ .$$
 (9)

In this work, we approach the propagation of errors by studying the Pauli fidelities associated with the repeated channel  $\mathcal{E}^x = e^{x\Lambda}$ :

$$f_P(\mathcal{E}^x) = 1 - \left(2\sum_{\substack{Q\\QP = -PQ}} |h_Q|^2\right) x^2 - \left(2\sum_{\substack{j,Q\\QP = -PQ}} |\ell_{j,Q}|^2\right) x + \text{(higher order)}$$
 (10)

Notice that both sums above are performed over the Paulis which anti-commute with P, and the second sum is further performed over the Lindblad jumps' indices j. In Appendix A.1, we provide a proof of Eq. (10), and expand on the higher order terms. We can get effective Pauli error probabilities from repeated channel fidelities  $f_P(\mathcal{E}^x)$  by using the Walsh-Hadamard transform [49]

$$p(P|\mathcal{E}^x) = x^2 |h_P|^2 + x \sum_{j} |\ell_{j,P}|^2 + \text{(higher order)}.$$
 (11)

The proof of Eq. (11) for Pauli fidelities of repeated channels is summarized in Appendix A.2. We refer to  $|h_P|^2$  as the coherent contribution to the error P. To a good approximation, coherent errors first induce a purely quadratic error growth as opposed to the purely linear initial growth characteristic to decoherent errors. This difference in propagation speed is the key to differentiating the two error sources.

## 3 Learning the Error Profile Attached to a Cycle

In this section, we provide the background material necessary to understand a CB-structured error characterization scheme known as Cycle Error Reconstruction (CER), which is also known as k-body Noise Reconstruction (KNR). Once the basics of CER are covered, we shall introduce our extension to the protocol which complements the standard CER diagnostics with a measure of the coherent contribution to the error profile.

#### 3.1 Cycle Error Reconstruction (CER) Error Diagnostic Protocol

In quantum computing, there are typically hard and easy cycles, which usually consist of parallel entangling gates and parallel single-qubit gates respectively. Hard cycles dictate the circuit performance compared to easy cycles. A dressed cycle refers to a composite cycle comprising a hard cycle followed (or preceded) by an easy cycle.

CER specifically provides error profiles attached to cycles relevant to circuits performed under Randomized Compiling (RC), a well-known error suppression technique [50–54]. To understand RC, consider a noisy application circuit composed of m sequential dressed cycles  $C_i$  interleaved with cycle-dependent error channels  $\mathcal{E}_i$ ,

$$\tilde{\mathcal{C}} = \mathcal{E}_m C_m \cdots \mathcal{E}_1 C_1 \ . \tag{12}$$

RC replaces the above application circuit  $\tilde{\mathcal{C}}$  meant to be run  $N_{\text{shots}}$  randomly sampled equivalent circuits (over a structured distribution of circuits), each to be run  $N_{\text{shots}}/n_{\text{rand}}$  times. The effect of RC is to effectively replace each noisy dressed cycle  $\mathcal{E}_i C_i$  with what is referred to as an effective dressed cycle  $\mathcal{E}_i^{\text{RC}}C_i$ , which is similar to  $\mathcal{E}_iC_i$ . The difference here is that the generic error channel  $\mathcal{E}_i$  is replaced with a Pauli stochastic error channel  $\mathcal{E}_i^{\text{RC}}$  of the form

$$\mathcal{E}_i^{\text{RC}}[\rho] = \sum_{P \in \mathbb{P}_n} p_i(P) P \rho P^{\dagger} , \qquad (13)$$

where  $\mathbb{P}_n$  is the *n*-qubit Pauli group, and where  $\{p_i(P)\}_P$  is a probability distribution over Pauli errors P corresponding with the ith cycle. The error distribution naturally depends on the cycle  $C_i$ .

CER specifically learns information about the distribution  $\{p_i(P)\}_P$ . To avoid scalability limitations, CER doesn't usually try to learn every probability value  $p_i(P)$ , because there are  $4^n$  of them. Instead, it learns marginal error probabilities over constrained unions of instruction labels. That is, if we let  $\mathbb{A}$  be a union of instruction labels (e.g.  $\{1\} \cup \{2,3\}$ ), and let  $\mathbb{A}^c$  be its complement over the architecture (e.g.  $\{4, \dots, n\}$ ), then the marginal probability of the error P (e.g. XXZ) over  $\mathbb{A}$  is defined as

$$\mu_{\mathbb{A}}(P) := \sum_{Q} p(P \text{ over } \mathbb{A} \text{ and } Q \text{ over } \mathbb{A}^c) .$$
 (14)

CER is tomographically complete since learning all marginals is equivalent to learning the probability distribution  $\{p_i(P)\}_P$ . However, due to locality constraints in realistic error models, poly(n) marginals are often sufficient to accurately reconstruct the error profile of a given cycle.

The marginal error probabilities associated with the stochastic channel  $\mathcal{E}_i^{\text{RC}}$  are retrieved from the *Pauli fidelities*, defined in Eq. (9). That is, given an effective cycle of interest  $\mathcal{E}^{\text{RC}}C$ , the CER protocol involves the estimation of a set of various Pauli fidelities,  $\{f_P(\mathcal{E}^{\text{RC}})\}_P$ , and converts the cycle of interest into a marginal error distribution. The Pauli fidelities are themselves extracted from circuit-level observables.

To be more explicit, let's specify CER circuits with three parameters, namely a set of commuting Paulis,  $\mathbb{S}$ , which is dictated by a state preparation and measurement (SPAM) strategy, a number of dressed cycle repetitions "m", and a string "s" sampled from a random variable X, which contains the information about the RC-randomized dressings. The role of the three parameters can be visualized in Fig. 1 (set x = 1), where the random string s dictates a choice of easy cycles. Each sampled CER circuit  $\tilde{\mathcal{C}}(\mathbb{S}, m, s)$  yields a set of fidelity-like numbers  $\{f_P^{\text{circuit}}(m, s)\}_{P \in \mathbb{S}}$  associated with the set  $\mathbb{S}$  of commuting Pauli operators determined by the SPAM strategy. The expectation of  $f_P^{\text{circuit}}(m, s)$  over the strings s in X obeys a decay formula of the form:

$$\mathbb{E}_s f_P^{\text{circuit}}(m, s) = A_P \left( f_P(\mathcal{E}^{\text{RC}}) \right)^m , \qquad (15)$$

where the constant  $A_P$  depends on SPAM errors, and where  $\mathcal{E}^{RC}$  is the Pauli stochastic error channel associated with the effective dressed cycle of interest. In practice, the LHS of Eq. (15) is replaced by a sample mean, and the Pauli fidelities  $f_P(\mathcal{E}^{RC})$  are obtained by gathering sample mean estimators for various values of dressed cycle repetitions m.

#### 3.2 An extension to CER to learn coherent contributions to errors

CER is meant to provide a diagnostic of effective RC cycles. Let the implementation of a hard cycle be expressed as the product  $C_H \circ \mathcal{E}_H$ , where  $\mathcal{E}_H$  is the cycle error channel attached to the ideal cycle implementation  $C_H$ . Similarly, let n-qubit Pauli easy cycles  $Q \in \mathbb{P}_n$  be expressed as the product  $\mathcal{E}_Q \circ Q$  (error channels can be placed on the left or right of the ideal implementation without loss of generality, but may differ depending on which side is chosen). To a high approximation, the fidelities given by CER correspond to [34]:

$$f_P^{\text{CER}} = f_P \left( \mathcal{E}_H \circ \left\langle \mathcal{E}_Q \right\rangle_{Q \in \mathbb{P}_n} \right) ,$$
 (16)

and it corresponds to the Pauli fidelities of the effective dressed cycle  $\mathcal{E}^{RC}C_H$  to the ideal cycle  $C_H$ . Notice that those fidelities don't provide a quantitative budgeting of the coherent and decoherent contributions to the infidelity.

To distinguish coherent error contributions from decoherent ones, we propose to perform CER sequences on folded hard cycles  $(\mathcal{E}_H \circ C_H)^x$  where  $C_H^x = C_H$ , for various values of x. The circuit representation of the experiments can be visualized in Fig. 1.

This idea is not generally equivalent to considering  $\mathcal{E}_H^x \circ C_H$ , but as we shall see, it is often very close. Let c be the smallest integer such that  $C_H^c = I$ , also referred to as the cyclicity of  $C_H$ . For instance, if the hard cycle consists of parallel CNOTs, we get c = 2 since CNOT is self-inverting. Without loss of generality, let's express  $\mathcal{E}_H$  as

$$\mathcal{E}_H =: \exp\left(\Lambda_H\right) =: \exp\left(\Lambda_H^{(0)} + \Lambda_H^{(1)} + \dots + \Lambda_H^{(c-1)}\right) , \qquad (17)$$

where the components  $\Lambda_H^{(j)}$  phase-commute with  $C_H$  according to the following equation:

$$\Lambda_H^{(j)} \circ C_H = e^{\frac{j}{c}2\pi i} \cdot C_H \circ \Lambda_H^{(j)} . \tag{18}$$

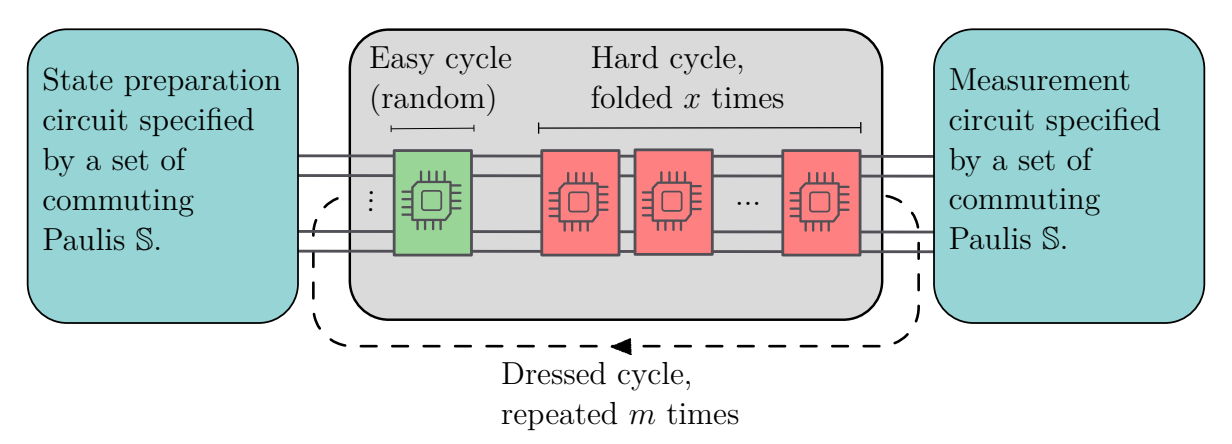


Figure 1: Visual representation of the CB-structured circuits in our error diagnostic scheme. The core cycles in gray are wrapped in state preparation and measurement (SPAM) circuits specified by a set of commuting Paulis  $\mathbb S$ . Dressed cycles are repeated m times and they each contain the x-folded hard cycle of interest  $(E_H \circ C_H)^x$ , where  $C_H^x = C_H$ . The easy cycles are randomized (the random aspect of the circuit is specified by a randomly sampled string s) but chosen together with m and the SPAM circuits such that the whole circuit amounts to a Pauli (which is accounted for in post-processing).

Now, let's consider multiplying the error channel  $\mathcal{E}_H$  with itself a number of K times where K is a multiple of the cyclicity c:

$$(C_H \circ \mathcal{E}_H)^K = \exp\left(K\Lambda_H^{(0)} + \frac{K}{c} \sum_{j=0}^{c-1} e^{\frac{j}{c}2\pi i} \Lambda_H^{(1)} + \dots + \frac{K}{c} \sum_{j=0}^{c-1} e^{\frac{c-1}{c}j2\pi i} \Lambda_H^{(c-1)}\right) + \text{(h.o.)} ,$$

$$= \exp\left(K\Lambda_H^{(0)}\right) + \text{(higher order)}$$
(19)

were the higher-order terms (h.o.) are dictated by the Baker-Campbell-Hausdorf formula [55], and are negligible to a good approximation for small enough integer K. Notice through Eq. (17) that  $\exp\left(\Lambda_H^{(0)}\right)$  is the component of  $\mathcal{E}_H$  that commutes with  $C_H$ . Therefore, Equation (19) essentially states that by folding the noisy cycle  $\mathcal{E}_H \circ C_H$ , we effectively evolve the component of  $\mathcal{E}_H$  that commutes with  $C_H$ . This often consists of the only substantial error component. Indeed,  $\mathcal{E}_H \circ C_H = C_H \circ \mathcal{E}_H$  is usually a good approximation if the hard cycle of interest  $C_H$  consists of a round of parallel pulses, since weak non-commuting noise components are expected to be echoed out by the drive, similarly as in Eq. (19).

By performing CER sequences on folded hard cycles  $(\mathcal{E}_H \circ C_H)^x$  where  $C_H^x = C_H$ ,

we effectively get an experiment to obtain the following fidelities using Eq. (19).

$$f_P^{\text{CER}}(x) = f_P \left( C_H^{-1} \circ (C_H \circ \mathcal{E}_H)^x \circ \langle \mathcal{E}_Q \rangle_{Q \in \mathbb{P}_n} \right) ,$$

$$= f_P \left( \exp \left( x \Lambda_H^{(0)} + \Lambda_H^{(1)} + \dots + \Lambda_H^{(c-1)} \right) \circ \langle \mathcal{E}_Q \rangle_{Q \in \mathbb{P}_n} \right) + (\text{higher order})$$

$$= f_P \left( \exp \left( x \Lambda_H^{(0)} \right) \circ \langle \mathcal{E}_Q \rangle_{Q \in \mathbb{P}_n} \right) + \epsilon_{\Lambda_H} + (\text{higher order}) , \qquad (20)$$

where the constant deviation  $\epsilon_{\Lambda_H}$  is zero if  $\mathcal{E}_H \circ C_H = C_H \circ \mathcal{E}_H$  (equivalently if  $\Lambda_H = \Lambda_H^{(0)}$ ). Standard CER fidelities from Eq. (16) are obtained by choosing x = 1. Finally, we wish to factor out the infidelity contribution from the average easy cycle error channel  $\langle \mathcal{E}_Q \rangle_{Q \in \mathbb{P}_n}$ :

$$f_P^{\text{CER}}(x) = f_P\left(\exp\left(x\Lambda_H^{(0)}\right)\right) + \epsilon_{\text{easy}}(x) + \epsilon_{\Lambda_H} + (\text{higher order}),$$
 (21)

where the infidelity contribution from the easy cycle is implicitly defined as  $\epsilon_{\text{easy}}(x)$ . Notice that this contribution can take the form of a constant plus a linear term in x. The linear dependence in x can arise if the easy cycle coherently interferes with the folded error  $\exp\left(x\Lambda_H^{(0)}\right)$ . However, since single-qubit gates are usually much less error-prone than entangling cycles,  $\epsilon_{\text{easy}}(x)$  has little effect on the infidelity profile.

Combining Eq. (21) with the results of Sections 2 and 3.1, we get that by performing CER sequences on folded hard cycles  $(\mathcal{E}_H \circ C_H)^x$  where  $C_H^x = C_H$ , we should expect decay formulas of the form:

$$\mathbb{E}_{s} f_{P}^{\text{circuit}}(m, x, s) = A_{P} \left( 1 - \left( 2 \sum_{\substack{Q \\ QP = -PQ}} |h_{Q}|^{2} \right) x^{2} - \left( 2 \sum_{\substack{j,Q \\ QP = -PQ}} |\ell_{j,Q}|^{2} \right) x + \epsilon(x) \right)^{m},$$
(22)

where the Hamiltonian and Lindbladian components are defined as in Eqs. (8a) and (8b), but are to be associated with the  $\Lambda_H^{(0)}$  effective Lindbladian that commutes with  $C_H$ , and where  $\epsilon(x) := \epsilon_{\text{easy}}(x) + \epsilon_{\Lambda_H}$  is a linear function of x that is expected to have little impact on the fidelity.

Finally, the coherent contributions  $|h_P|^2$  to the error probabilities  $p(P|\mathcal{E}_H)$  of the hard cycle  $C_H$  are obtained by gathering the quadratic components from Eq. (22) and by performing the Walsh-Hadamard transform.

# 4 Extracting Coherent and Decoherent Qubit Errors Using CER

In this section, we elaborate on a simple example of the CER extension protocol introduced in Section 3.2. This allows us to expand further on the subtleties of the fitting model such as the properties of the underlying covariance matrix. Finally, we provide numerical evidence that the error profile obtained from our suggested experiment matches the underlying error model.

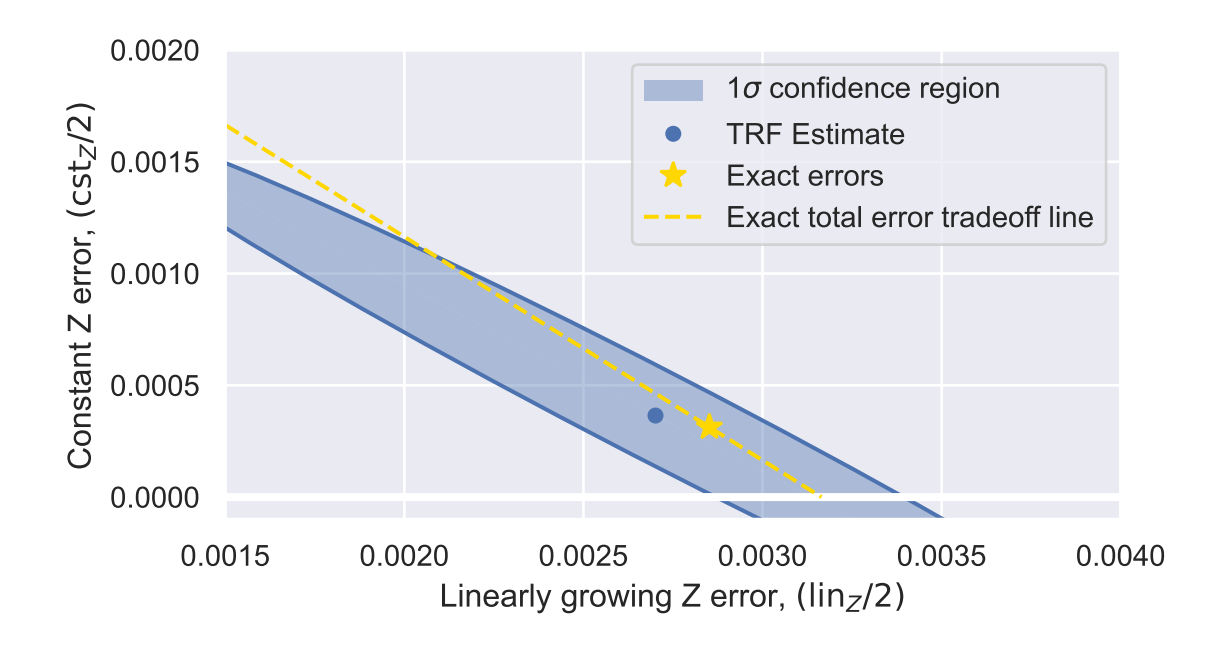


Figure 2: The blue cropped ellipse represents the  $1\sigma$  confidence region of 2 fitted parameters, namely  $\ln_Z/2$  and  $\mathrm{cst}_P/2$ , based on the covariance matrix returned by the fitting function. These 2 parameters appear in the 12-parameter model given by Eq. (23). Recall that those parameters are physically constrained to be positive, hence the cropping of the region. The fit was performed on simulated data in order to include exact values (see Section 4.2). The solid blue dot is the value returned by the fit, and the star is the exact value of the parameter pair. The dotted line represent a tradeoff line where  $(\ln_Z + \mathrm{cst}_P)/2$  is set to the exact value, for different values of  $\ln_Z$  and  $\mathrm{cst}_Z$ . The longer principal axis of the ellipse in the figure is nearly aligned with the dotted tradeoff line. This illustrates that the estimate of  $(\ln_Z + \mathrm{cst}_P)/2$  is much more precise than the estimate of  $(\ln_Z - \mathrm{cst}_P)/2$ .

# 4.1 Fitting Model

As discussed in Section 3.2, our experiment consists of sampling CER circuits for various circuit parameter tuples  $(x, m, \mathbb{B}, s)$ :

- x is the number of folded hard cycle per dressed cycle;
- m is the number of dressed cycles;
- $\mathbb{B}$  denotes a state and preparation and measurement (SPAM) basis as a set of commuting Pauli observables. We omit  $\mathbb{B}$  in the expression of the Pauli fidelities since it is implicit chosen through the P Pauli index.
- s denotes a randomly sampled string that encodes the random part of the circuit construction for the fixed parameters  $(x, m, \mathbb{B})$ .

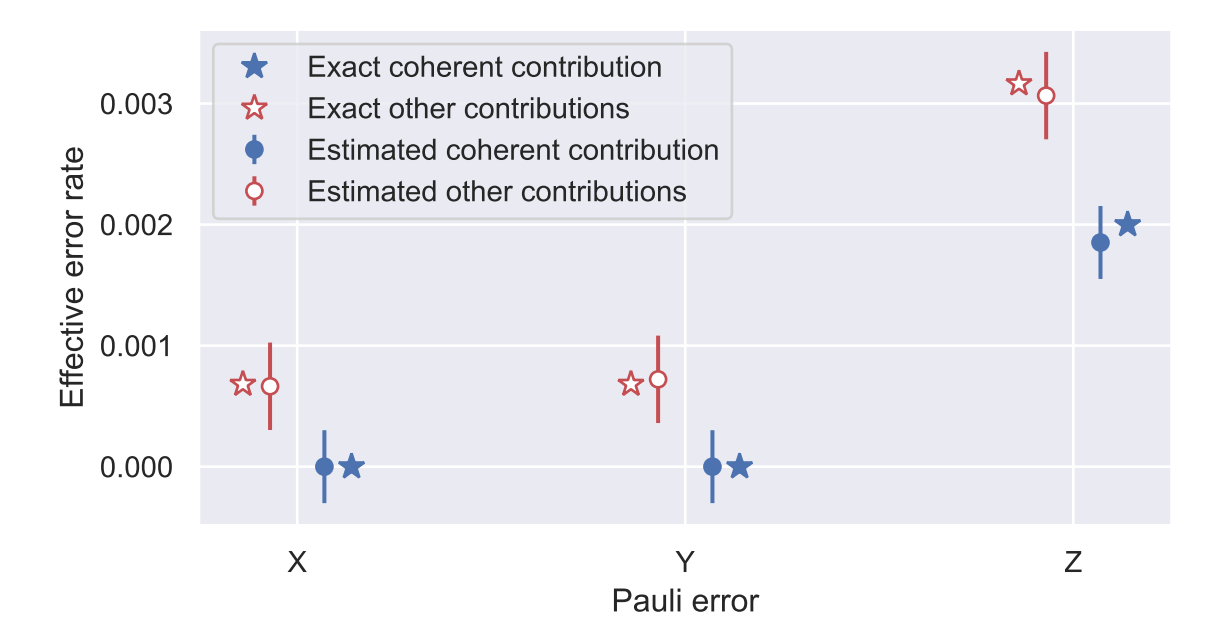


Figure 3: Error profile obtained from a simulation of our experiment. For the simulated error model, we used the relaxation times from  $ibmq\_montreal$ , and introduced a coherent Z error with effective rate of 0.002.

From those parameterized sampled circuits, we generated fidelity-like quantities  $f_P^{\text{circuit}}(x, m, s)$ . Consider the simplest instance of such an experiment on a single qubit. According to Eq. (22), the sample average of  $f_P^{\text{circuit}}(x, m, s)$  obeys the following 12-parameter decay model:

$$\mathbb{E}_{s} f_{X}^{\text{circuit}}(x, m, s) = A_{X} \left( 1 - (\operatorname{quad}_{Y} + \operatorname{quad}_{Z}) x^{2} - (\operatorname{lin}_{Y} + \operatorname{lin}_{Z}) x - (\operatorname{cst}_{Y} + \operatorname{cst}_{Z}) \right)^{m}$$

$$\mathbb{E}_{s} f_{Y}^{\text{circuit}}(x, m, s) = A_{Y} \left( 1 - (\operatorname{quad}_{X} + \operatorname{quad}_{Z}) x^{2} - (\operatorname{lin}_{X} + \operatorname{lin}_{Z}) x - (\operatorname{cst}_{X} + \operatorname{cst}_{Z}) \right)^{m}$$

$$\mathbb{E}_{s} f_{Z}^{\text{circuit}}(x, m, s) = A_{Z} \left( 1 - (\operatorname{quad}_{X} + \operatorname{quad}_{Y}) x^{2} - (\operatorname{lin}_{X} + \operatorname{lin}_{Y}) x - (\operatorname{cst}_{X} + \operatorname{cst}_{Y}) \right)^{m}$$

$$(23)$$

In the general case, for N different Pauli fidelities to estimate, the number of parameters in the fit becomes 4N. Since CER focuses on error probabilities marginalized over a small number of qubits, the number of parameters is guaranteed to be manageable unless we observe long-range error correlations.

As shown in the previous section, the coefficients  $quad_P$  appearing in the quadratic part of the exponential decay are in direct correspondence with the effective coherent contribution to the infidelity of the hard cycle on the qubit:

$$quad_P = 2|h_P|^2. (24)$$

The linear coefficients are most realistically in correspondence with the decoherent contribution to the infidelity of the hard cycle on the qubit, although some linear effects could in principle be induced by a coherent effect between the randomized easy cycle and the folded hard cycle. Easy cycles are usually much less error-prone than hard cycles, meaning that the linear coefficient is often entirely dominated by the decoherent contribution. Finally, the constant terms  $cst_P$  are due to the errors occurring during the easy cycles, as well as to the components of the hard cycle error that does not commute with the hard cycle  $C_H$  (see Eq. (21)).

#### 4.2 Fitting Model Simulation Results and Analysis

To anticipate our hardware-based experiments, we perform numerical simulations of our experiment in the simple case of a single qubit subject to a noise source coming from a nearby entangling gate. To measure the systematic increase in the magnitude of the error from the noise, the number of CNOT gates is systematically increased. Measurements are taken for hard gate cycles of 1, 3, 5, 7 and 9 CNOT gates and the simulations are run for 20,000 shots per random circuit. For the simulated error model, we use the relaxation times from  $ibmq\_montreal$ , and introduce a coherent Z error with an effective rate of 0.002 to simulate the presence of coherent crosstalk.

In our numerical analysis, we notice that  $\lim_P$  and  $\operatorname{cst}_P$  are strongly anti-correlated, inducing a large uncertainty for their difference  $\lim_P - \operatorname{cst}_P$ . This is well illustrated in Fig. 2, where we can further see that the sum  $\lim_P + \operatorname{cst}_P$  is estimated with high precision and accuracy. For this reason, we contrast the coherent contribution to the error rates with the sum of the other contributions (see Fig. 3). In the regime where the twirling operations are nearly perfect, the contributions  $\lim_P + \operatorname{cst}_P$  can be interpreted as the sole result of decoherence during the hard cycle. More generally, one could make tighter upper-bounds on the constants  $\operatorname{cst}_P$ , based on physical assumptions or on additional benchmarking data. For example, in Fig. 2, one could reduce the uncertainty on the difference  $\lim_P - \operatorname{cst}_P$  by upper-bounding the constant Z error  $\operatorname{cst}_Z/2 \leq 0.0005$ . This would crop the confidence region and improve the precision and level of detail of the error profile, but would inherently rely on an assumption.

In all of the computations, the error parameters appearing in the model described by Eq. (23) are bounded between 0 and 1 (they are usually close to 0). As such, we use the Trust-Region-Reflective (TRF) least mean squares algorithm to fit the parameters to the data [56]. We compare the estimated error profile to an exact reference in Fig. 3 and find a satisfactory degree of agreement.

# 5 Hardware results and analysis

We test our experiment design derived in Section 3.2 on cloud-accessible IBM hardware as a proof-of-concept. Our choice of cycle and marginal distribution to reconstruct is inspired by the circuits used to probe the spin-spin correlation function of a Heisenberg

spin chain [57]. These types of circuits are in fact what launched the idea of this work. Fig. 4 is a block diagram of the spin-spin correlation function circuit showing CNOT gates in the circuit and an ancilla qubit used to measure the computational results. Fig. 5 shows a more detailed sub-circuit used in the time evolution of the Heisenberg spin-chain.

As shown through the diagrams, the types of circuits that we consider feature a spectator ancillary qubit that is left idling during the trotterized evolution of the spin chain. As such, we focused our interest on the coherent and decoherent error profile marginalized on this ancilla. In this simple instance, the hard cycle of interest consist of a CNOT acting on a pair of qubits neighboring to the idle ancilla. We implement the circuit on three different IBM quantum computing hardware platforms (ibmq\_guadalupe, ibmq\_montreal, and ibmq\_manila). Appendix B discusses the specific circuit implementations on each of the hardware platforms.

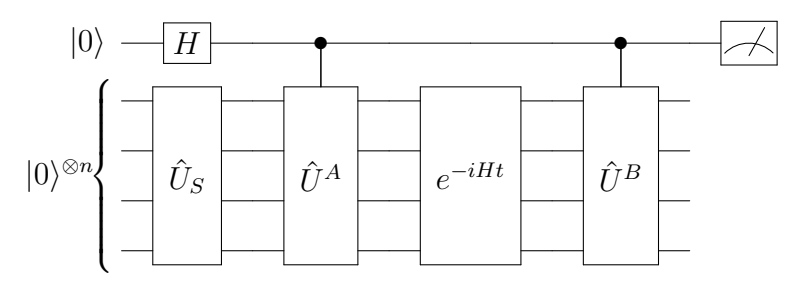


Figure 4: Block diagram for calculating spin-spin correlation in 4-site Heisenberg spin-chain [57].

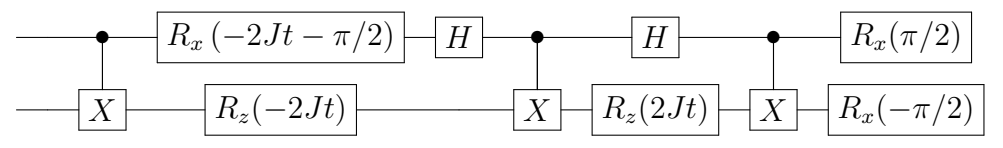


Figure 5: Sub-circuit used in time-evolution (see  $e^{-iHt}$  block of Fig. 4) of the 4-site Heisenberg spin-chain.

Starting with the proposed fitting model discussed in Section 4.1 we note that each of the quadratic equations  $f_X$ ,  $f_Y$  and  $f_Z$  in Eq. (23) are interconnected because each direction (X, Y, Z) has anti-commuting terms for X, Y, and Z that are coupled across each dimension of the model. This requires each of the coefficients in the polynomial to have both a coherent  $(quad_i)$  and a decoherent  $(lin_i)$  fitting parameter. Having all possible terms that anti-commute with each of the x, y, and z axes in Eq. (23) included in the proposed model require twelve parameters ( $3"A_{X,Y,Z}"$  parameters, 3  $"quad_{X,Y,Z}"$  parameters, 3 " $lin_{X,Y,Z}"$  parameters and finally 3 " $cst_{X,Y,Z}"$  parameters). One advantage of such an approach is that the global fit to these twelve parameters assures overall positive error rates. The results from this global fitting produce 75 values (five different CNOT repetitions at the five different sequence lengths and three  $f_X$ ,  $f_Y$  and  $f_Z$ ).

We construct a graph of the component fidelities  $f_X$ ,  $f_Y$  and  $f_Z$  versus sequence lengths for hard cycle CNOT repetitions 1, 3, 5, 7, and 9 for the fitting model for each of the three different hardware platforms. On each graph, we plot the 75 data points with star symbols ( $\star$ ). Fig. 6 shows the data plotted for the ibmq\_manila hardware platform.

The next step is to include the results from the CER computations. These calculations are randomly compiled 30 times with different Paulis for each sequence length on each of the three hardware platforms using 10,000 shots for  $ibmq_manila$  and 20,000 shots for  $ibmq_guadalupe$  and  $ibmq_montreal$ . We then color-code each of the 30 results for each sequence length and plot them on the graph of  $f_X$ ,  $f_Y$  and  $f_Z$  versus sequence lengths for each hard cycle CNOT repetition (1, 3, 5, 7, and 9) for each of the three different hardware platforms. We also plot the sample mean from the 30 different data points for each hard cycle CNOT repetition at each sequence length on the graph with the diamond symbol( $\diamond$ ) and a standard deviation error bar. Fig. 6 shows these results for the  $ibmq_manila$  hardware platform. We construct similar computations and graphs for both  $ibm_montreal$  and  $ibm_guadalupe$ .

Upon examination of Fig. 6 in more detail, it can be seen that some of the 75 different pairs of stars and diamonds do not overlay each other on the graph. For example, the 3 CNOT folding star-diamond pairs for all of the sequence lengths 4, 8, 12, 16, and 32 in the component fidelity  $f_Y$  are displaced from each other. Similar examples of these star-diamond pair displacements can also be seen throughout the other CNOT foldings in the figure.

We then implement a minimization procedure on the star-diamond data. The goal is to globally minimize the distance between the diamond values and the star values for all 75 star-diamond combinations. We perform this global minimization by computing the square of the difference between each pair of stars and diamonds and dividing by that specific star value and then summing over all 75 star/diamond pairs This calculation is essentially a  $\chi^2$  minimization of the goodness of the proposed fit in order to extract each of the power-law coefficients for the proposed equation modelling the coherent and decoherent error rates.

We can write the power-law coefficients using Eq. (22) as:

$$\mathbb{E}_s f_P^{\text{circuit}}(x, m, s) = A_P \left( 1 - a_P x^2 - b_P x - c_P \right)^m, \tag{25}$$

The coefficients from the  $\chi^2$  minimization procedure on the data can be mapped to the terms in Eq. (22) for a given Pauli P. These terms can be defined as

$$a_P := |h_P|^2 := 2 \sum_{QP = -PQ} |h_Q|^2$$
 (26)

for the coherent (quadratic) term,

$$b_P := \sum_{j} |\ell_{j,P}|^2 := 2 \sum_{\substack{j,Q \\ QP = -PQ}} |\ell_{j,Q}|^2$$
 (27)

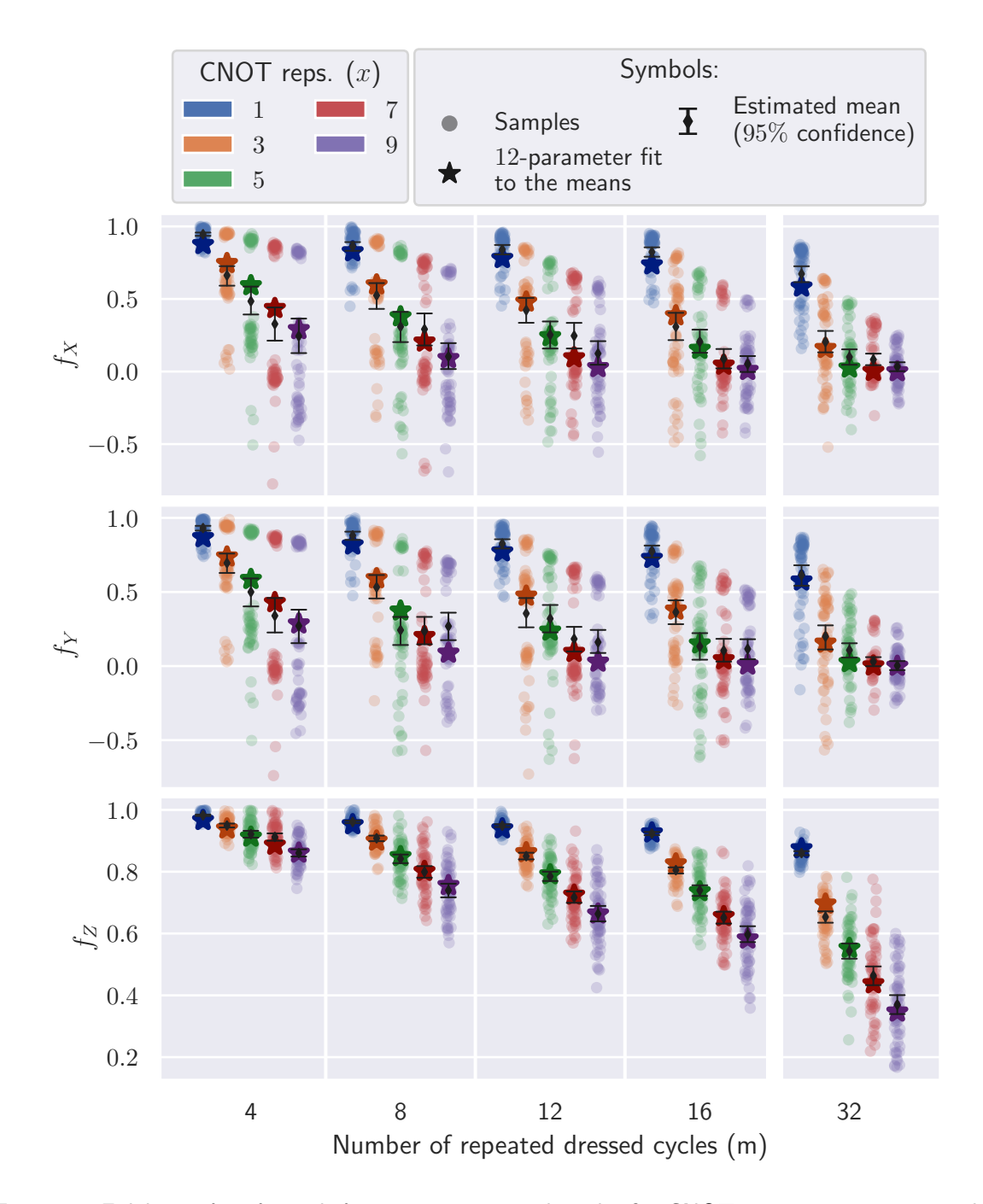


Figure 6: Fidelities  $f_X$ ,  $f_Y$  and  $f_Z$  versus sequence lengths for CNOT repetition 1,3,5,7, and 9 for ibmq\_manila. Each CNOT repetition is color coded and identified in the legend in the upper left portion of the figure. Each CNOT repetition was randomly compiled 30 times with different Paulis at each sequence length. Each individual data point plotted is color code matched to the corresponding CNOT repetition. The average value from the 30 different data points for each CNOT repetition at each sequence length is then plotted on the graph with the diamond symbol( $\diamond$ ) and standard deviation error bar. The global fitting from the model produces 75 values for the estimated mean and is plotted with star symbols ( $\star$ )

for the decoherent (linear) term and

$$c_P := \epsilon(x) \tag{28}$$

for the coefficient. We plot these terms for each of the three IBM hardware platforms as shown in Fig. 7. This figure is the central result of this research project and shows the effective error rate versus Pauli Error (X, Y and Z) for the designated single qubit on each of the hardware platforms. These results as well as the data from the simulator are shown in Table 1.

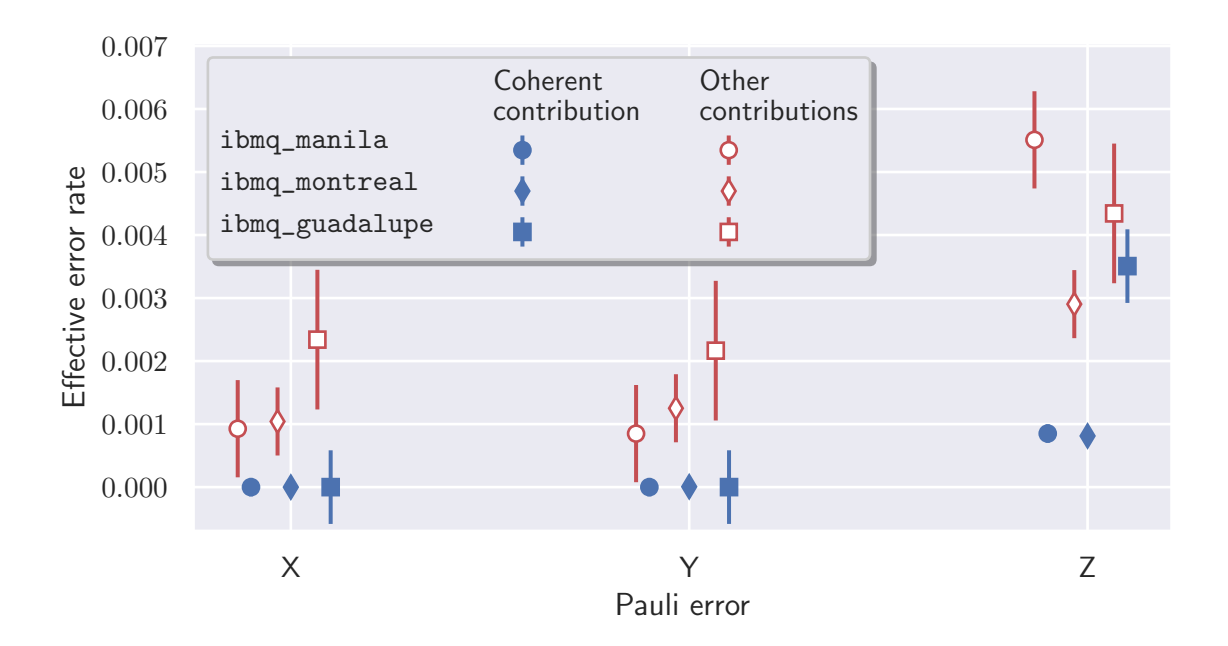


Figure 7: Effective error profile for an idling ancilla standing next to a CNOT on IBM hardware platforms ibm\_guadalupe, ibm\_montreal and ibm\_manila. The horizontal axis contains the three possible Pauli errors on the ancilla, and the vertical axis quantifies the respective effective error probability (when rendering the error channel Pauli stochastic through a projection). The solid blue markers indicate the coherent contribution to the error rate, while the red open markers quantify the other contributions to the error rate. The results are obtained via the extended CER protocol described in Section 3. The numerical values of the error rates with their respective uncertainty are contained in Table 2.

From Section 4.2 a more detailed analysis for the 12-parameter fit shows that the sums and differences of the  $\lim_{P}/2$  and  $\operatorname{cst}_{P}/2$  are strongly anti-correlated. The  $\operatorname{quad}_{P}/2$  values contain the coherent contribution to the error rate, while the  $(\lim_{P} + \operatorname{cst}_{P})/2$  contains the other contributions. We compute the adjusted parameter fit values for each of the three IBM hardware platforms for the Paulis X, Y and Z and also for the simulator and the results are summarized in Table 2. The table clearly shows that the Pauli Z  $\lim_{P}/2$  and  $\operatorname{cst}_{P}/2$  terms have the strongest error measured on the single qubit on each of the hardware platforms.

It is well-known that the static ZZ coupling in a transmon qubit is always present and leads to both coherent and incoherent errors [58]. Recent works have theoretically analyzed the effect of crosstalk on simultaneous gate operation in a tunable ZZ coupling-based qubit architecture [59, 60].

Our results confirmed that a CNOT gate indeed affects the idling qubit, and the nature of the coherent error is predominantly Pauli Z error. We observed this noise bias toward Pauli Z error due to the effects of static ZZ coupling in a transmon qubit.

This increase in the single qubit error as the number of CNOT hard cycles is increased can also be seen graphically through heat map plots for the single qubit on  $ibm\_guadalupe$ ,  $ibm\_montreal$  and  $ibm\_manila$  as shown in Fig. 9, Fig. 10 and Fig. 11 in Appendix C. Although there is some increase in the X and Y Pauli error, these heatmaps also graphically illustrate that it it the Z Pauli error that show the greatest increase as the number of CNOT hard cycles increases. We observe from our heatmaps that Pauli Z error increases rapidly compared to X and Y errors when the number of CNOTs increases from 1 to 9. This rapid scaling of Z error is the signature of coherent errors. Thus, our characterization scheme shows not only that Pauli Z error is the dominant error on the IBM quantum processors, but also that a substantial fraction of it is the result of coherent processes.

# 6 Summary

We successfully demonstrate the design and implementation of an efficient and scalable diagnostic method that quantitatively differentiates between coherent and decoherent errors in cycles. The characterization scheme that we suggest in the present work differs from existing error diagnostic methods such as GST [37–42] in that it is targeted toward the characterization of the effective dressed cycles present in in randomly compiled circuits. This is an important tool because many error suppression techniques implemented today only provide improved circuit performance by focusing on mitigating either decoherent or coherent errors. Our method can therefore be used to measure the impact of error suppression suites on the type of errors that they specifically target.

We leverage a CB-structured error characterization protocol known as CER [1, 34, 45]. The original method was designed to measure the error profile on effective dressed cycles, which are tailored to have purely decoherent errors via a compiling method known as RC [35]. We expand on the basic CER method by introducing an additional hyper-parameter (labeled x in this work) which corresponds to the number of hard cycle repetitions before being subject to Pauli twirling (see Fig. 1). This additional hyper-parameter allows for quantitative estimates of the coherent error contributions to be computed through a generalization of the fidelity decay formula (Eq. (22)).

Our data analysis relies on the different propagation formulas of coherent and decoherent errors in folded error channels (see Section 2). As a proof of concept, we test our method both physically and numerically by reconstructing the effective error profile on a single-qubit ancilla left idling during a cycle. The numerical simulation confirms a strong agreement between the error profile estimated by our protocol and the exact underlying error model. The data obtained from IBM hardware platforms (ibmq\_guadalupe, ibmq\_manila, and ibmq\_montreal) revealed a substantial level of coherent errors occurring on the idling ancilla induced by an entangling operation (see Fig. 7).

In terms of next steps, we note that the fitting method derived in the current work only relies on the sample averages of fidelities, and does not take into consideration the shape of the distribution of the fidelities for fixed (m, x) hyper-parameters. As shown in Fig. 6, coherent errors affect more properties of the fidelity distributions than just the mean and we leave as an open problem the refining of the fitting function based on those considerations, as well as statistical optimization of the choice of hyper-parameters. Finally, we leave the demonstration of our proposed CB-structured method as a means to design and benchmark error suppression tools for future work.

fidelity	$A_P$	$a_P$	$b_P$	$c_P$
Montreal				
$f_X$	1.00(2)	0.0016(8)	0.008(2)	0.000(2)
$f_Y$	0.98(2)	0.0016(7)	0.007(2)	0.000(2)
$f_Z$	1.00(1)	0.00001(8)	0.0038(7)	0.000(1)
Guadalupe				
$f_X$	0.96(3)	0.007(2)	0.013(8)	0.000(7)
$f_Y$	0.95(3)	0.007(2)	0.011(8)	0.003(7)
$f_Z$	0.96(2)	0.0000(1)	0.006(8)	0.003(2)
Manila				
$f_X$	0.93(3)	0.0017(4)	0.013(3)	0.000(3)
$f_Y$	0.92(3)	0.0017(4)	0.013(3)	0.000(4)
$f_Z$	0.93(1)	0.00000(9)	0.0036(8)	0.000(2)
Simulator				
$f_X$	1.000(4)	0.0037(9)	0.007(5)	0.001(4)
$f_Y$	0.997(4)	0.0037(8)	0.006(4)	0.001(4)
$f_Z$	1.0000(8)	0.00000(1)	0.0024(1)	0.0004(1)

Table 1: Fitted parameters from Eq. (25). The lower-case parameters correspond to the coefficients of the quadratic equation inside the fidelity decays.

## 7 Acknowledgments

P.D. was supported in part by the U.S. Department of Energy (DoE) under award DE-AC05-00OR22725. S.K.R. acknowledges financial support from the J. William Fulbright Foreign Scholarship Board and the Fulbright Commission in India (USIEF) through a

Pauli error	$\operatorname{quad}_P/2$	$lin_P/2$	$\operatorname{cst}_P/2$	$(\ln_P + \operatorname{cst}_P)/2$	$(\lim_P - \operatorname{cst}_P)/2$
Montreal					
X	0.00000(9)	0.008(2)	0.0004(9)	0.0010(5)	0.000(1)
Y	0.00001(9)	0.007(2)	0.0000(9)	0.0013(5)	0.001(1)
Z	0.00081(9)	0.0038(7)	0.0000(9)	0.0029(5)	0.003(1)
Guadalupe					
X	0.0000(6)	0.001(3)	0.001(3)	0.002(1)	0.000(6)
Y	0.0000(6)	0.002(3)	0.000(3)	0.002(1)	0.002(6)
Z	0.0035(6)	0.004(3)	0.000(3)	0.004(1)	0.004(6)
Manila					
X	0.0000(1)	0.001(1)	0.000(1)	0.0009(8)	0.001(2)
Y	0.0000(1)	0.001(1)	0.000(1)	0.0008(8)	0.001(2)
Z	0.0008(1)	0.006(1)	0.000(1)	0.0055(8)	0.006(2)
Simulator					
X	0.0000(3)	0.000(2)	0.000(1)	0.0007(4)	0.000(3)
Y	0.0000(3)	0.001(2)	0.000(1)	0.0007(4)	0.001(3)
Z	0.0019(1)	0.003(2)	0.000(1)	0.0031(4)	0.002(3)

Table 2: Various fitted parameters corresponding to the 12-parameter model presented in Eq. (23), for three different hardware platforms. We include the difference and the sum of  $\lim_P/2$  and  $\operatorname{cst}_P/2$  since these parameters are strongly anti-correlated (see Section 4.2). From Eq. (24), we get that the  $\operatorname{quad}_P/2$  column contains the coherent contribution to the error rate, while the  $(\lim_P + \operatorname{cst}_P)/2$  contains the other contributions. These error rates are shown in Fig. 7.

Fulbright Nehru Doctoral Research Fellowship 2021-2022. We acknowledge the use of IBM Quantum services for this work. The views expressed are those of the authors, and do not reflect the official policy or position of IBM or the IBM Quantum team. We thank North Carolina State University (NCSU) for access to the IBM Quantum Network quantum computing hardware platforms through the NCSU IBM Quantum Hub. The project team acknowledges the use of True-Q software from Keysight Technologies.

#### 8 Author Contributions

All authors contributed equally to this project.

# 9 Competing interests

A. C-D. has a financial interest in Keysight Technology Inc. and the use of True-Q software. P.D. and S.K.R. declare no competing interests.

# 10 Data Availability

Data is available from the corresponding author upon reasonable request.

# References

- [1] Alexander Erhard, Joel J Wallman, Lukas Postler, Michael Meth, Roman Stricker, Esteban A Martinez, Philipp Schindler, Thomas Monz, Joseph Emerson, and Rainer Blatt. Characterizing large-scale quantum computers via cycle benchmarking. *Nature communications*, 10(1):1–7, 2019.
- [2] John Preskill. Quantum computing in the NISQ era and beyond. Quantum, 2:79, 2018.
- [3] H. Y. Carr and E. M. Purcell. Effects of Diffusion on Free Precession in Nuclear Magnetic Resonance Experiments. *Physical Review*, 94(3):630–638, May 1954. DOI: 10.1103/PhysRev.94.630.
- [4] S. Meiboom and D. Gill. Modified Spin-Echo Method for Measuring Nuclear Relaxation Times. *Review of Scientific Instruments*, 29(8):688–691, August 1958. DOI: 10.1063/1.1716296.
- [5] Lorenza Viola and Seth Lloyd. Dynamical suppression of decoherence in two-state quantum systems. *Phys. Rev. A*, 58(4):2733–2744, October 1998. DOI: 10.1103/PhysRevA.58.2733.
- [6] Lorenza Viola, Emanuel Knill, and Seth Lloyd. Dynamical Decoupling of Open Quantum Systems. *Phys. Rev. Lett.*, 82(12):2417–2421, March 1999. DOI: 10.1103/PhysRevLett.82.2417.
- [7] Lorenza Viola, Seth Lloyd, and Emanuel Knill. Universal Control of Decoupled Quantum Systems. *Phys. Rev. Lett.*, 83(23):4888–4891, December 1999. DOI: 10.1103/PhysRevLett.83.4888.
- [8] Lorenza Viola and Emanuel Knill. Robust Dynamical Decoupling of Quantum Systems with Bounded Controls. *Phys. Rev. Lett.*, 90(3):037901, January 2003. DOI: 10.1103/PhysRevLett.90.037901.
- [9] K. Khodjasteh and D. A. Lidar. Fault-Tolerant Quantum Dynamical Decoupling. *Phys. Rev. Lett.*, 95(18):180501, October 2005. DOI: 10.1103/Phys-RevLett.95.180501.
- [10] Götz S. Uhrig. Keeping a Quantum Bit Alive by Optimized  $\pi$ -Pulse Sequences. *Phys. Rev. Lett.*, 98(10):100504, March 2007. DOI: 10.1103/Phys-RevLett.98.100504.
- [11] Jacob R. West, Daniel A. Lidar, Bryan H. Fong, and Mark F. Gyure. High Fidelity Quantum Gates via Dynamical Decoupling. *Phys. Rev. Lett.*, 105(23):230503, December 2010. DOI: 10.1103/PhysRevLett.105.230503.
- [12] Wen Yang, Zhen-Yu Wang, and Ren-Bao Liu. Preserving qubit coherence by dynamical decoupling. *Frontiers of Physics*, 6(1):2–14, March 2011. DOI: 10.1007/s11467-010-0113-8.

- [13] Ying Li and Simon C. Benjamin. Efficient variational quantum simulator incorporating active error minimization. *Phys. Rev. X*, 7:021050, Jun 2017. DOI: 10.1103/PhysRevX.7.021050. URL https://link.aps.org/doi/10.1103/ PhysRevX.7.021050.
- [14] Kristan Temme, Sergey Bravyi, and Jay M. Gambetta. Error mitigation for short-depth quantum circuits. *Phys. Rev. Lett.*, 119:180509, Nov 2017. DOI: 10.1103/PhysRevLett.119.180509. URL https://link.aps.org/doi/10.1103/ PhysRevLett.119.180509.
- [15] E. F. Dumitrescu, A. J. McCaskey, G. Hagen, G. R. Jansen, T. D. Morris, T. Papenbrock, R. C. Pooser, D. J. Dean, and P. Lougovski. Cloud quantum computing of an atomic nucleus. *Phys. Rev. Lett.*, 120:210501, May 2018. DOI: 10.1103/Phys-RevLett.120.210501. URL https://link.aps.org/doi/10.1103/PhysRevLett.120.210501.
- [16] Suguru Endo, Simon C. Benjamin, and Ying Li. Practical quantum error mitigation for near-future applications. *Phys. Rev. X*, 8:031027, Jul 2018. DOI: 10.1103/PhysRevX.8.031027. URL https://link.aps.org/doi/10.1103/ PhysRevX.8.031027.
- [17] Tudor Giurgica-Tiron, Yousef Hindy, Ryan LaRose, Andrea Mari, and William J. Zeng. Digital zero noise extrapolation for quantum error mitigation. In 2020 IEEE International Conference on Quantum Computing and Engineering (QCE), pages 306–316, 2020. DOI: 10.1109/QCE49297.2020.00045.
- [18] Andre He, Benjamin Nachman, Wibe A. de Jong, and Christian W. Bauer. Zeronoise extrapolation for quantum-gate error mitigation with identity insertions. *Phys. Rev. A*, 102:012426, Jul 2020. DOI: 10.1103/PhysRevA.102.012426. URL https://link.aps.org/doi/10.1103/PhysRevA.102.012426.
- [19] Zhenyu Cai. Multi-exponential error extrapolation and combining error mitigation techniques for NISQ applications. npj Quantum Information, 7(1), may 2021. DOI: 10.1038/s41534-021-00404-3. URL https://doi.org/10.1038% 2Fs41534-021-00404-3.
- [20] Zhenyu Cai. A practical framework for quantum error mitigation. 2021. DOI: 10.48550/ARXIV.2110.05389. URL https://arxiv.org/abs/2110.05389.
- [21] Zhenyu Cai. Resource-efficient purification-based quantum error mitigation. 2021. DOI: 10.48550/ARXIV.2107.07279. URL https://arxiv.org/abs/2107.07279.
- [22] Armands Strikis, Dayue Qin, Yanzhu Chen, Simon C. Benjamin, and Ying Li. Learning-based quantum error mitigation. PRX Quantum, 2:040330, Nov 2021. DOI: 10.1103/PRXQuantum.2.040330. URL https://link.aps.org/doi/10.1103/PRXQuantum.2.040330.
- [23] William J. Huggins, Jarrod R. McClean, Nicholas C. Rubin, Zhang Jiang, Nathan Wiebe, K. Birgitta Whaley, and Ryan Babbush. Efficient and noise resilient measurements for quantum chemistry on near-term quantum computers. npj Quantum Information, 7(1), feb 2021. DOI: 10.1038/s41534-020-00341-7. URL https://doi.org/10.1038%2Fs41534-020-00341-7.

- [24] Bá lint Koczor. The dominant eigenvector of a noisy quantum state. New Journal of Physics, 23(12):123047, dec 2021. DOI: 10.1088/1367-2630/ac37ae. URL https://doi.org/10.1088%2F1367-2630%2Fac37ae.
- [25] Bálint Koczor. Exponential error suppression for near-term quantum devices. *Phys. Rev. X*, 11:031057, Sep 2021. DOI: 10.1103/PhysRevX.11.031057. URL https://link.aps.org/doi/10.1103/PhysRevX.11.031057.
- [26] Thomas E. O'Brien, Stefano Polla, Nicholas C. Rubin, William J. Huggins, Sam McArdle, Sergio Boixo, Jarrod R. McClean, and Ryan Babbush. Error mitigation via verified phase estimation. *PRX Quantum*, 2:020317, May 2021. DOI: 10.1103/PRXQuantum.2.020317. URL https://link.aps.org/doi/10.1103/PRXQuantum.2.020317.
- [27] Samuele Ferracin, Akel Hashim, Jean-Loup Ville, Ravi Naik, Arnaud Carignan-Dugas, Hammam Qassim, Alexis Morvan, David I. Santiago, Irfan Siddiqi, and Joel J. Wallman. Efficiently improving the performance of noisy quantum computers. 2022. DOI: 10.48550/ARXIV.2201.10672. URL https://arxiv.org/abs/2201.10672.
- [28] Mingxia Huo and Ying Li. Dual-state purification for practical quantum error mitigation. *Phys. Rev. A*, 105:022427, Feb 2022. DOI: 10.1103/PhysRevA.105.022427. URL https://link.aps.org/doi/10.1103/PhysRevA.105.022427.
- [29] Zhenyu Cai, Ryan Babbush, Simon C. Benjamin, Suguru Endo, William J. Hug-gins, Ying Li, Jarrod R. McClean, and Thomas E. O'Brien. Quantum error mitigation. 2022. DOI: 10.48550/ARXIV.2210.00921. URL https://arxiv.org/abs/2210.00921.
- [30] Tomochika Kurita, Hammam Qassim, Masatoshi Ishii, Hirotaka Oshima, Shintaro Sato, and Joseph Emerson. Synergetic quantum error mitigation by randomized compiling and zero-noise extrapolation for the variational quantum eigensolver. 2022. DOI: 10.48550/ARXIV.2212.11198. URL https://arxiv.org/abs/2212.11198.
- [31] Daniel Bultrini, Max Hunter Gordon, Esperanza Lopez, and German Sierra. Simple mitigation strategy for a systematic gate error in ibmq. arXiv preprint arXiv:2012.00831, 2020.
- [32] Adam Winick, Joel J. Wallman, and Joseph Emerson. Simulating and mitigating crosstalk. *Physical Review Letters*, 126(23), jun 2021. DOI: 10.1103/physrevlett.126.230502. URL https://doi.org/10.1103%2Fphysrevlett.126.230502.
- [33] Muhammad Ahsan, Syed Abbas Zilqurnain Naqvi, and Haider Anwer. Quantum circuit engineering for correcting coherent noise. *Physical Review A*, 105(2), feb 2022. DOI: 10.1103/physreva.105.022428. URL https://doi.org/10.1103%2Fphysreva.105.022428.
- [34] Arnaud Carignan-Dugas, Dar Dahlen, Ian Hincks, Egor Ospadov, Stefanie J. Beale, Samuele Ferracin, Joshua Skanes-Norman, Joseph Emerson, and Joel Wallman. The learning and compiled calibration of cycle errors in quantum computing architectures in preparation. arXiv, Mar 2023.

- [35] Joel J Wallman and Steven T Flammia. Randomized benchmarking with confidence. New Journal of Physics, 16(10):103032, 2014.
- [36] Adam Winick, Joel J. Wallman, Dar Dahlen, Ian Hincks, Egor Ospadov, and Joseph Emerson. Concepts and conditions for error suppression through randomized compiling. 2022. DOI: 10.48550/ARXIV.2212.07500. URL https://arxiv.org/abs/2212.07500.
- [37] Seth T. Merkel, Jay M. Gambetta, John a. Smolin, Stefano Poletto, Antonio D. Córcoles, Blake R. Johnson, Colm a. Ryan, and Matthias Steffen. Self-consistent quantum process tomography. *Physical Review A*, 87(6):062119, June 2013. ISSN 1050-2947. DOI: 10.1103/PhysRevA.87.062119. URL http://link.aps.org/doi/10.1103/PhysRevA.87.062119.
- [38] Robin Blume-Kohout, John King Gamble, Erik Nielsen, Jonathan Mizrahi, Jonathan D. Sterk, and Peter Maunz. Robust, self-consistent, closed-form tomography of quantum logic gates on a trapped ion qubit. *ArXiv e-prints*, art. arXiv:1310.4492, October 2013.
- [39] Robin Blume-Kohout, John King Gamble, Erik Nielsen, Kenneth Rudinger, Jonathan Mizrahi, Kevin Fortier, and Peter Maunz. Demonstration of qubit operations below a rigorous fault tolerance threshold with gate set tomography. *Nature Communications*, 8(1), feb 2017. DOI: 10.1038/ncomms14485. URL https://doi.org/10.1038%2Fncomms14485.
- [40] Daniel Greenbaum. Introduction to quantum gate set tomography. 2015. DOI: 10.48550/ARXIV.1509.02921. URL https://arxiv.org/abs/1509.02921.
- [41] Erik Nielsen, John King Gamble, Kenneth Rudinger, Travis Scholten, Kevin Young, and Robin Blume-Kohout. Gate set tomography. Quantum, 5:557, oct 2021. DOI: 10.22331/q-2021-10-05-557. URL https://doi.org/10.22331% 2Fq-2021-10-05-557.
- [42] Raphael Brieger, Ingo Roth, and Martin Kliesch. Compressive gate set tomography. 2021. DOI: 10.48550/ARXIV.2112.05176. URL https://arxiv.org/abs/2112.05176.
- [43] Steven T. Flammia and Joel J. Wallman. Efficient estimation of Pauli channels. arXiv e-prints, art. arXiv:1907.12976, July 2019.
- [44] Jonas Helsen, Joel J. Wallman, Steven T. Flammia, and Stephanie Wehner. Multiqubit randomized benchmarking using few samples. *Phys. Rev. A*, 100:032304, Sep 2019. DOI: 10.1103/PhysRevA.100.032304. URL https://link.aps.org/doi/10.1103/PhysRevA.100.032304.
- [45] Arnaud Carignan-Dugas, Dar Dahlen, Ian Hincks, Egor Ospadov, Stefanie J. Beale, Samuele Ferracin, Joshua Skanes-Norman, Joseph Emerson, and Joel Wallman. The learning and compiled calibration of cycle errors in quantum computing architectures. In APS March Meeting, 2022.
- [46] Joel J. Wallman. Systems and methods for reconstructing noise from pauli fidelities, November 17 U.S. patent 10838792, Nov. 2020. URL https://patents. justia.com/patent/10838792.

- [47] Ziang Yu and Yingzhou Li. Analysis of error propagation in quantum computers. arXiv preprint arXiv:2209.01699, 2022.
- [48] G. Lindblad. On the generators of quantum dynamical semigroups. Communications in Mathematical Physics, 48(2):119 130, 1976. DOI: cmp/1103899849. URL https://doi.org/.
- [49] Michael A. Nielsen and Isaac L. Chuang. Quantum Computation and Quantum Information: 10th Anniversary Edition. Cambridge University Press, 2010. DOI: 10.1017/CBO9780511976667.
- [50] Joel J Wallman and Joseph Emerson. Noise tailoring for scalable quantum computation via randomized compiling. *Physical Review A*, 94(5):052325, 2016.
- [51] Akel Hashim, Ravi K. Naik, Alexis Morvan, Jean-Loup Ville, Bradley Mitchell, John Mark Kreikebaum, Marc Davis, Ethan Smith, Costin Iancu, Kevin P. O'Brien, Ian Hincks, Joel J. Wallman, Joseph Emerson, and Irfan Siddiqi. Randomized compiling for scalable quantum computing on a noisy superconducting quantum processor. *Phys. Rev. X*, 11:041039, Nov 2021. DOI: 10.1103/Phys-RevX.11.041039. URL https://link.aps.org/doi/10.1103/PhysRevX.11.041039.
- [52] Jean-Loup Ville, Alexis Morvan, Akel Hashim, Ravi K Naik, Marie Lu, Bradley Mitchell, John-Mark Kreikebaum, Kevin P O'Brien, Joel J Wallman, Ian Hincks, et al. Leveraging randomized compiling for the qite algorithm. arXiv preprint arXiv:2104.08785, 2021.
- [53] Yanwu Gu, Yunheng Ma, Nicolo Forcellini, and Dong E Liu. Noise-resilient phase estimation with randomized compiling. arXiv preprint arXiv:2208.04100, 2022.
- [54] Adam Winick, Joel J Wallman, Dar Dahlen, Ian Hincks, Egor Ospadov, and Joseph Emerson. Concepts and conditions for error suppression through randomized compiling. arXiv preprint arXiv:2212.07500, 2022.
- [55] Lie Groups, Lie Algebras, and Representations An Elementary Introduction. Springer. ISBN 978-3-319-13466-6.
- [56] Pauli Virtanen, Ralf Gommers, Travis E. Oliphant, Matt Haberland, Tyler Reddy, David Cournapeau, Evgeni Burovski, Pearu Peterson, Warren Weckesser, Jonathan Bright, Stéfan J. van der Walt, Matthew Brett, Joshua Wilson, K. Jarrod Millman, Nikolay Mayorov, Andrew R. J. Nelson, Eric Jones, Robert Kern, Eric Larson, C J Carey, İlhan Polat, Yu Feng, Eric W. Moore, Jake VanderPlas, Denis Laxalde, Josef Perktold, Robert Cimrman, Ian Henriksen, E. A. Quintero, Charles R. Harris, Anne M. Archibald, Antônio H. Ribeiro, Fabian Pedregosa, Paul van Mulbregt, and SciPy 1.0 Contributors. SciPy 1.0: Fundamental Algorithms for Scientific Computing in Python. Nature Methods, 17:261–272, 2020. DOI: 10.1038/s41592-019-0686-2.
- [57] Akhil Francis, JK Freericks, and AF Kemper. Quantum computation of magnon spectra. *Physical Review B*, 101(1):014411, 2020.
- [58] V Tripathi, H Chen, M Khezri, KW Yip, EM Levenson-Falk, and DA Lidar. Suppression of crosstalk in superconducting qubits using dynamical decoupling (2021). arXiv preprint arXiv:2108.04530.

- [59] Peng Zhao, Kehuan Linghu, Zhiyuan Li, Peng Xu, Ruixia Wang, Guangming Xue, Yirong Jin, and Haifeng Yu. Quantum crosstalk analysis for simultaneous gate operations on superconducting qubits. *PRX Quantum*, 3(2):020301, 2022.
- [60] Junling Long, Tongyu Zhao, Mustafa Bal, Ruichen Zhao, George S Barron, Hsiangsheng Ku, Joel A Howard, Xian Wu, Corey Rae H McRae, Xiu-Hao Deng, et al. A universal quantum gate set for transmon qubits with strong zz interactions. arXiv preprint arXiv:2103.12305, 2021.
- [61] Albert W. Marshall, Ingram Olkin, and Barry C. Arnold. *Inequalities: Theory of Majorization and its Applications*, volume 143. Springer, second edition, 2011. DOI: 10.1007/978-0-387-68276-1.
- [62] Stefanie J. Beale, Kristine Boone, Arnaud Carignan-Dugas, Anthony Chytros, Dar Dahlen, Hillary Dawkins, Joseph Emerson, Samuele Ferracin, Virginia Frey, Ian Hincks, David Hufnagel, Pavithran Iyer, Aditya Jain, Jason Kolbush, Egor Ospadov, José Luis Pino, Hammam Qassim, Jordan Saunders, Joshua Skanes-Norman, Andrew Stasiuk, Joel J. Wallman, Adam Winick, and Emily Wright. True-q, June 2020. URL https://doi.org/10.5281/zenodo.3945250.
- [63] Andrew Wack, Hanhee Paik, Ali Javadi-Abhari, Petar Jurcevic, Ismael Faro, Jay M. Gambetta, and Blake R. Johnson. Quality, speed, and scale: three key attributes to measure the performance of near-term quantum computers, 2021. URL https://arxiv.org/abs/2110.14108.

## A Supplementary Material

#### A.1 Derivation of the Pauli Fidelities of a Repeated Channel

In this section, we prove lemma 1, which yields the propagation formula given in Eq. (10). Before, consider the following definition:

**Definition 1** (Area of Effect). Consider a connectivity graph G = (V, E), where V is the set of qubit vertices and E is a set of connectivity edges. We say that, given the graph G, an operator M as an area of effect

$$A\left(M|G\right) := \min_{W \subset V} |W| \tag{29}$$

such that

- 1. The vertex-induced subgraph obtained by limiting the vertices of G to the set W is connected;
- 2. M can be expressed as  $M_{H_W} \otimes I_{H_{W^c}}$ , where  $W^c$  is the complement of W, and  $H_w$  ( $H_{W^c}$ ) denotes the Hilbert space over the qubits in the set W ( $W^c$ ).

An operator M is said to be geometrically (or topologically) k-local if A(M|G) = k. As we show, if we limit the area of effect of noisy interactions, early-truncated Taylor expansion of  $e^{\Lambda}$  will be appropriate for approximating the effect of  $e^{\Lambda}$  on reasonably small subsystems.

#### Lemma 1: Pauli fidelities of repeated channel

Let Lindbladian and Hamiltonian operators be at most geometrically k-local for some small integer k. Consider an error channel  $\mathcal{E} = e^{\Lambda}$  stemming from geometrically k-local interactions. The fidelity of P associated with the channel  $\mathcal{E}^x = e^{x\Lambda}$  is given by

$$f_{P}(x) = 1 - \left(2 \sum_{\substack{Q \\ QP = -PQ}} |h_{Q}|^{2}\right) x^{2} - \left(2 \sum_{\substack{j,Q \\ QP = -PQ}} |\ell_{j,Q}|^{2}\right) x + O\left((1 - f_{P}(x))^{2} \operatorname{poly}(e^{k})\right).$$
(30)

*Proof.* A way to interpret the total evolution  $e^{\Lambda}$  is to consider  $\Lambda$  as a transition matrix. The total evolution depicted by  $e^{\Lambda}$  is then the sum over all paths, and each path is weighted by 1/J! where J is the number of jumps. The first part of the proof will be to quantify and categorize the transition amplitudes, and the second part will be to sum up the different paths. For conciseness, we omit the graph dependence in the area of effect function, i.e. A(M|G) is replaced by A(M).

Part I: Quantifying and categorizing the transition amplitudes

Let's define the transition amplitude from the Pauli  $P \in \mathbb{P}_n$  to the Pauli  $Q \in \mathbb{P}_n$  as

$$t_{P \to Q} := \frac{\text{Tr}\left(Q\Lambda[P]\right)}{2^n} \ . \tag{31}$$

From the definition of the Lindblad matrix Eq. (5), we more specifically get

$$2^{n} \cdot t_{P \to Q} = -i \operatorname{Tr} \left( Q[H, P] \right) + \sum_{j} \left\{ \operatorname{Tr} \left( QL_{j}PL_{j}^{\dagger} \right) - \frac{1}{2} \operatorname{Tr} \left( QPL_{j}^{\dagger}L_{j} \right) - \frac{1}{2} \operatorname{Tr} \left( QL_{j}^{\dagger}L_{j}P \right) \right\} . \tag{32}$$

It follows by the hermicity-preserving nature of the evolution that  $t_{P\to Q}$  remains real. Let's decompose the operators  $L_j$  Eq. (33a),  $L_j^{\dagger}$  Eq. (33b) and H Eq. (33c) by inserting summations over the Pauli operators S as follows:

$$L_j = \sum_{S} \ell_{j,S} S , \qquad (33a)$$

$$L_j^{\dagger} = \sum_{S} \ell_{j,PQS}^* PQS , \qquad (33b)$$

$$H = \sum_{S} h_{PS} PS , \qquad (33c)$$

where

$$\ell_{j,S} := \text{Tr}(SL_j)/2^n , \qquad (34a)$$

$$\ell_{i,POS} := \text{Tr}(PQSL_i)/2^n , \qquad (34b)$$

$$h_{PS} := \operatorname{Tr}((PS)^{\dagger}H)/2^{n} , \qquad (34c)$$

and let's substitute those decompositions into Eq. (32):

$$t_{P\to Q} = -ih_{PQ} \operatorname{Tr} \left( QPQP - QPPQ \right) / 2^n + \sum_{j,S} \ell_{j,S} \ell_{j,PQS}^* \operatorname{Tr} \left( QSPPQS \right) / 2^n$$
$$- \frac{1}{2} \sum_{j,S} \ell_{j,S} \ell_{j,PQS}^* \operatorname{Tr} \left( (PQ + QP)PQSS \right) / 2^n . \tag{35}$$

The above expression can be further simplified. Let's define the commutation function,

$$\chi_{P,Q} = \begin{cases} 1 \text{ if } P \text{ and } Q \text{ commute }, \\ -1 \text{ if } P \text{ and } Q \text{ anti-commute }. \end{cases}$$
 (36)

By using the commutation function and by taking the real projection of  $t_{P\to Q}$ , we get

$$t_{P\to Q} = -\operatorname{Real}(ih_{PQ})(\chi_{P,Q} - 1) + \sum_{j,S} \operatorname{Real}\left(\ell_{j,S}\ell_{j,PQS}^*\right) \left(\chi_{Q,S} - \frac{\chi_{P,Q} + 1}{2}\right) , \quad (37)$$

which can be broken in three cases.

Case 1: P = Q (i.e.  $t_{P \to P}$ )

In the case where P = Q, we find

$$t_{P \to P} = \sum_{j,S} \operatorname{Real} \left( \ell_{j,S} \ell_{j,S}^* \right) \left( \chi_{P,S} - 1 \right)$$

$$= -2 \sum_{\substack{S \\ \chi_{P,S} = -1 \\ A(S) < k}} \sum_{j} |\ell_{j,S}|^2 . \tag{38}$$

Notice that the sum above has 2 constraints, namely  $\chi_{P,S} = -1$  and  $A(S) \leq k$ . With these, the number of terms in the sum of Eq. (38) scales proportionally to the weight w(P) of P, and scales exponentially in k and in the level of connectivity of the architecture's graph G.

Notice from this case that we already have that:

$$\frac{d}{dx}f_P(x)\Big|_{0} = t_{P\to P} = -2\sum_{\substack{S\\\chi_{P,S} = -1\\A(S) \le k}} \sum_{j} |\ell_{j,S}|^2 . \tag{39}$$

Case 2: PQ = QP and  $P \neq Q$ 

First, if PQ = QP, then  $\chi_{P,Q} = 1$  and we get

$$t_{P \to Q} = \sum_{j,S} \operatorname{Real} \left( \ell_{j,S} \ell_{j,PQS}^* \right) \left( \chi_{Q,S} - 1 \right),$$

$$= -2 \sum_{\substack{S \\ \chi_{Q,S} = -1 \\ A(S + PQS) \le k}} \sum_{j} \operatorname{Real} \left( \ell_{j,S} \ell_{j,PQS}^* \right) . \tag{40}$$

The transition amplitude is still scaling as the squared magnitude of the Lindbladian terms. Applying the Cauchy-Schwarz inequality to the transition amplitude Eq. (41), we get:

$$|t_{P\to Q}| = 2 \left| \sum_{\substack{XQ,S=-1\\A(S+PQS)\leq k}} \sum_{j} \mathbb{R}eal\left(\ell_{j,S}\ell_{j,PQS}^*\right) \right|,$$

$$\leq 2 \sum_{\substack{XQ,S=-1\\A(S+PQS)\leq k}} \sqrt{\sum_{j} |\ell_{j,S}|^2} \sqrt{\sum_{j} |\ell_{j,PQS}|^2}$$

$$(41)$$

Since PQ = QP, we find that PQS anti-commutes with Q. Therefore, it follows from majorization inequalities that [61]:

$$|t_{P\to Q}| \le 2 \sum_{\substack{S \ \chi_{Q,S}=-1 \ A(S+PQS)\le k}} \sum_{j} |\ell_{j,S}|^2 .$$
 (42)

The number of terms in the sum over S is constrained since

- 1. S has to anti-commute with the transition endpoint Q (i.e. SQ = -QS);
- 2. S + PQS has to be geometrically k-local (i.e.  $A(S + PQS) \le k$ );

Since  $PQ \neq I$ , the second condition implies that non-zero transitions must obey  $A(PQ) \leq k$ ; in simpler terms, Q must differ from P by a k-local operator. To get a better picture of non-zero transitions, imagine P as a product of different "Pauli islands", defined as follows:

**Definition 2** (Pauli Islands). A Pauli P is said to be a k-island if any tensor product partitioning  $P = Q \otimes R$  obeys

$$A(P|G) < A(Q|G) + A(R|G) + k - 1$$
. (43)

Any Pauli P can be partitioned into a product of islands, and this product is unique. For instance, for k=2 and a chain topology,  $P=(X_2X_3X_4)\otimes(Z_6Y_7)$  is a product of two islands.

**Rules 1** (Transition rules for PQ = QP). The allowed transitions must obey the following rules:

- 1. From the onset, PQ = QP and  $Q \neq P$ .
- 2. An allowed transition is the creation of a new geometrically k-local island. For instance with our  $P = (X_2 X_3 X_4) \otimes (Z_6 Y_7)$  example, we could have an endpoint of the form  $Q = (X_2 X_3 X_4) \otimes (Z_6 Y_7) \otimes (Y_{75})$ .
- 3. An allowed transition can be the geometrically k-local modification of a single island. Still with our  $P = (X_2X_3X_4) \otimes (Z_6Y_7)$  example, we could have an endpoint of the form  $Q = (Y_1X_2X_3X_4) \otimes (Z_6Y_7)$  or  $Q = (X_2X_3X_4) \otimes (X_6X_7)$ .
- 4. The annihilation of an island is forbidden! This is because of the first constraint on S, which states that it must anti-commute with Q, and enforces S to connect to the endpoint Q.
- 5. Through the second rule, islands that are less than 2k edges apart can be merged via island modifications. Still with our  $P = (X_2X_3X_4) \otimes (Z_6Y_7)$  example, we could have a single island endpoint:  $Q = (X_2X_3X_4Y_5Z_6Y_7)$ .

By looking carefully at the above rules, notice that for a non-zero double transition  $t_{P\to Q}t_{Q\to P}$  to start and end at P and pass by Q such that QP=PQ, it has to be a geometrically k-local modification of a single island (see Rules 1, item 3). The reason for this is that although island creations have non-zero amplitudes, annihilation transitions are prohibited. Only a few triple transitions  $t_{P\to Q}t_{Q\to R}t_{R\to P}$  can start and end with P and involve an island creation: 1) start with an island creation that is within 2k edges, 2) merge the created island to one of P's islands in the second transition, 3) return to P through a single island modification.

With this argument in mind, let's bound the total amplitude of double transitions  $t_{P\to Q}t_{Q\to P}$  that start and end at P and pass by Q such that QP=PQ:

$$\sum_{\substack{Q, \ \chi_{Q,P}=1, \\ \text{geo. } k\text{-local} \\ \text{mod. of 1 isl.}}} |t_{P\to Q}||t_{Q\to P}| \le 4 \sum_{\substack{Q, \ \chi_{Q,P}=1, \\ \text{geo. } k\text{-local} \\ \text{mod. of 1 isl.}}} \sum_{\substack{S' \\ \chi_{Q,S}=-1 \\ \chi_{Q,S'}=-1 \\ \chi_{Q$$

Notice that the constrained double sum over Q and S(S') goes over some k-local areas connected to P and over some k-local jumps in those regions. Therefore, up to a multiplicity constant  $\Gamma$  that grows exponentially in k, we get

$$\sum_{\substack{Q, \chi_{Q,P}=1, \text{geo. } k\text{-local} \\ \text{mod. of 1 isl}}} |t_{P\to Q}||t_{Q\to P}| \le \Gamma |t_{P\to P}| \max_{S} \left(\sum_{j} |\ell_{j,S}|^2\right) , \tag{45}$$

which, unless the noise is highly non-local (i.e.  $\Gamma$  is large), is much smaller than  $|t_{P\to P}|$ . Triple transitions can be similarly neglected compared to  $t_{P\to P}$  on the first order approximation.

Case 
$$3:PQ = -QP$$

Finally, if PQ = -QP, we get

$$t_{P\to Q} = 2\mathbb{R}\text{eal}(ih_{PQ}) + \sum_{i,S} \mathbb{R}\text{eal}\left(\ell_{j,S}\ell_{j,PQS}^*\right)\chi_{Q,S} . \tag{46}$$

From there we can deduce some transition rules:

**Rules 2** (Transition rules for PQ = -QP). The allowed transitions must obey the following rules:

- 1. Since P and Q must anti-commute, island creation and annihilation are both forbidden.
- 2. An allowed transition can be the geometrically k-local modification of a single island.

Using the fact that  $h_{PQ} = -h_{QP}$  and  $\chi_{PQ,P} = -1$ , we get:

$$\sum_{\substack{Q, \ \chi_{Q,P}=-1, \\ \text{geo. } k\text{-local} \\ \text{god. } \begin{cases} t_{P\to Q} t_{Q\to P} = -4 \\ \chi_{S,P}=-1 \end{cases}} t_{P\to Q} t_{Q\to P} = -4 \sum_{\substack{S \\ \chi_{S,P}=-1}} |h_S|^2 + T$$
(47)

where T is a term with a magnitude bounded as

$$|T| = \left| \sum_{\substack{Q, \ \chi_{Q,P} = -1, \\ \text{geo. } k\text{-local} \\ \text{mod. of 1 isl. }}} \sum_{\substack{S,S' \\ A(S+PQS) \leq k \\ \text{mod. of 1 isl. }}} \sum_{\substack{A(S+PQS) \leq k \\ A(S'+PQS') \leq k}} \mathbb{R} \operatorname{eal}\left(\ell_{i,S}\ell_{i,PQS}^*\right) \mathbb{R} \operatorname{eal}\left(\ell_{j,S}\ell_{j,PQS'}^*\right) \chi_{Q,S}\chi_{P,S'}$$

$$+ 2 \sum_{\substack{Q, \ \chi_{Q,P} = -1, \\ \text{geo. } k\text{-local} \\ \text{mod. of 1 isl.}}} \mathbb{R} \operatorname{eal}\left(ih_{PQ}\right) \sum_{\substack{S \\ A(S+PQS) \leq k}} \sum_{j} \mathbb{R} \operatorname{eal}\left(\ell_{j,S}\ell_{j,PQS}^*\right) \chi_{Q,S}\chi_{P,S'} \right|$$

$$\leq \left| \sum_{\substack{Q, \ \chi_{Q,P} = -1, \\ \text{geo. } k\text{-local} \\ \text{mod. of 1 isl.}}} \left(2 \left|h_{PQ}\right| + \sum_{\substack{S \\ A(S+PQS) \leq k}} \sum_{j} \left|\ell_{j,S}\right|^{2}\right) \left(\sum_{\substack{X_{Q}, \chi_{Q,P} = -1, \\ \text{geo. } k\text{-local} \\ \text{mod. of 1 isl.}}} \sum_{j} \left|\ell_{j,S}\right|^{2}\right) \right|$$

$$\leq \sum_{\substack{Q, \ \chi_{Q,P} = -1, \\ \text{geo. } k\text{-local} \\ \text{mod. of 1 isl.}}} \left(2 \left|h_{PQ}\right| + \sum_{\substack{S \\ A(S+PQS) \leq k}} \sum_{j} \left|\ell_{j,S}\right|^{2}\right) \left|\sum_{\substack{Q, \ \chi_{Q,P} = -1, \\ \text{geo. } k\text{-local} \\ \text{mod. of 1 isl.}}} \sum_{j} \left|\ell_{j,S}\right|^{2}\right|$$

$$= \sum_{\substack{Q, \ \chi_{Q,P} = -1, \\ \text{geo. } k\text{-local} \\ \text{mod. of 1 isl.}}} \sum_{j} \left|\ell_{j,S}\right|^{2}$$

$$= \sum_{\substack{Q, \ \chi_{Q,P} = -1, \\ \text{geo. } k\text{-local} \\ \text{mod. of 1 isl.}}} \sum_{j} \left|\ell_{j,S}\right|^{2}$$

where the second line was obtained by using

$$\left| \sum_{j,S} \operatorname{Real} \left( \ell_{j,S} \ell_{j,PQS}^* \right) \chi_{Q,S} \right| \leq \sum_{\substack{S \\ A(S+PQS) < k}} \sum_{j} |\ell_{j,S}|^2 . \tag{49}$$

Let S(P) be the support P (the qubits where the Paulis are non-trivial). The second factor in Eq. (48) scales as the average single transition  $t_{Q\to Q}$  over all Paulis Q with the same support as P:

$$\left| \sum_{\substack{Q, \ \chi_{Q,P}=-1, \ \text{geo. } k\text{-local } \\ \text{geo. } k\text{-local } \\ \text{mod of 1 isl}}} \sum_{\substack{S \\ A(S+PQS) \le k}} \sum_{j} |\ell_{j,S}|^2 \right| = O(\text{poly}(e^k)) \times \mathbb{E}_{\substack{Q \\ \mathbb{S}(Q) = \mathbb{S}(P)}} |t_{Q \to Q}| . \tag{50}$$

Using Eq. (39), this means that |T| can be bounded by

$$|T| \leq O(\operatorname{poly}(e^{k})) \times \left(2 \max_{S, \chi_{S,P}=-1} |h_{S}|\right) \times \left(\mathbb{E}_{\mathbb{S}(Q)=\mathbb{S}(P)} \left| \frac{d}{dx} f_{Q}(x) \right|_{0} \right) + O(\operatorname{poly}(e^{k})) \times \left(\max_{S} \sum_{j} |\ell_{j,S}|^{2}\right) \times \left(\mathbb{E}_{\mathbb{S}(Q)=\mathbb{S}(P)} \left| \frac{d}{dx} f_{Q}(x) \right|_{0} \right) . \tag{51}$$

Finally, notice that since  $t_{P\to Q}=-t_{Q\to P}$  for all P,Q such that  $\chi_{P,Q}=-1$ , the sum of triple transitions  $t_{P\to Q}t_{Q\to R}t_{R\to P}$  such that  $\chi_{Q,P}=\chi_{Q,R}=\chi_{R,P}=-1$  must sum to zero since  $t_{P\to R}t_{R\to Q}t_{Q\to P}=-t_{P\to Q}t_{Q\to R}t_{R\to P}$ . This means that the next terms to consider are quadruple transitions. The summed amplitude of these transistion is expressed as:

$$\sum_{\substack{Q, \ \chi_{Q,P}=-1, \\ \text{geo. } k\text{-local} \\ \text{mod. of 1 P isl. mod. of 1 Q isl. mod. of 1 R isl.}} \sum_{\substack{T, \ \chi_{R,T}=-1, \\ T, \ \chi_{R,T}=-1, \\$$

One way to bound the above sum is to use:

$$|t_{Q\to R}t_{R\to T}| \le \left(2\max_{S}|h_{S}| + \beta(k)\max_{S}\sum_{j}|\ell_{j,S}|^{2}\right)^{2},$$
 (53)

where  $\beta(k) = O(\text{poly}(k))$ . Since the number of terms in the sum  $\sum_{\substack{R, \chi_{Q,R} = -1, \text{geo. } k\text{-local} \\ \text{mod. of 1 Q isl.}}} \sum_{k} \sum_{\substack{R \in \mathcal{R} \\ \text{poly} \in \mathcal{R} \\ \text{of 2 local}}} \sum_{k} \sum_{\substack{R \in \mathcal{R} \\ \text{poly} \in \mathcal{R} \\ \text{of 3 local}}} \sum_{k} \sum_{\substack{R \in \mathcal{R} \\ \text{poly} \in \mathcal{R} \\ \text{of 3 local}}} \sum_{k}  

as  $O(\text{poly}(e^k))w(P)$ , we get

$$\sum_{\substack{Q,\ \chi_{Q,P}=-1,\\ \text{geo. $k$-local}}} \sum_{\substack{R,\ \chi_{Q,R}=-1,\\ \text{geo. $k$-local}}} \sum_{\substack{T,\ \chi_{R,T}=-1,\\ \text{geo. $k$-local}\\ \text{mod. of 1 P isl. mod. of 1 Q isl. mod. of 1 R isl.}} |t_{P\to Q}t_{Q\to R}t_{R\to T}t_{T\to P}|$$

$$\leq O(\operatorname{poly}(e^{k}))w(P) \left(2 \max_{S} |h_{S}| + \beta(k) \max_{S} \sum_{j} |\ell_{j,S}|^{2}\right)^{2} \left(\sum_{\substack{Q, \chi_{Q,P}=-1, \\ \text{geo. } k\text{-local} \\ \text{mod. of 1 P isl.}}} |t_{P \to Q}|\right)^{2} \\
\leq \left(O(\operatorname{poly}(e^{k}))w(P) \left(2 \max_{S} |h_{S}| + \beta(k) \max_{S} \sum_{j} |\ell_{j,S}|^{2}\right)\right)^{2} \sum_{\substack{Q, \chi_{Q,P}=-1, \\ \text{geo. } k\text{-local} \\ \text{mod. of 1 P isl.}}} |t_{P \to Q}|^{2} \\
\ll \left|\sum_{\substack{Q, \chi_{Q,P}=-1, \\ \text{geo. } k\text{-local} \\ \text{mod. of 1 isl.}}} t_{P \to Q} t_{Q \to P}\right|, \tag{54}$$

where the third line was obtained by using Holder's inequality and the fact that the number of term in the sum  $\sum_{\substack{Q, \chi_{Q,P}=-1, \text{geo. } k\text{-local} \\ \text{mod. of 1 P isl.}}} V(P)$ :

$$\sum_{\substack{Q, \ \chi_{Q,P}=-1, \\ \text{geo. } k\text{-local} \\ \text{mod. of 1 P isl.}}} |t_{P\to Q}| \le \sqrt{O(\text{poly}(e^k))w(P)} \sqrt{\sum_{\substack{Q, \ \chi_{Q,P}=-1, \\ \text{geo. } k\text{-local} \\ \text{mod. of 1 P isl.}}} |t_{P\to Q}|^2 \ . \tag{55}$$

#### A.2 Derivation of the Error Probabilities of a repeated channel

Error processes are not necessarily stochastic, meaning that it doesn't always make sense to discuss error probabilities. However, we can always project the error channels unto a stochastic one, and then consider the resulting error probability distribution. As such, we define the effective Pauli error probabilities as the resulting Pauli error probability of a channel once it is projected onto its Pauli stochastic component.

When it comes to Pauli stochastic channels, there is a duality between Pauli fidelities and Pauli error probabilities. The two are in fact related by a linear operation known as the Walsh-Hadamard transform. That is, if we consider a vector of fidelities,  $\mathbf{f}$  (such as  $\mathbf{f} = (f_I, f_X, f_Y, f_Z)$ ), we can obtain the vector of error probabilities  $\mathbf{e}e$  (such as  $\mathbf{e} = (e_I, e_X, e_Y, e_Z)$ ) via:

$$\mathbf{e} = W\mathbf{f},\tag{56}$$

where W is the Walsh-Hadamard matrix. The entry  $W_{ij}$  is 1 if the jth Pauli in the domain vector commutes with the ith Pauli in the image.  $W_{ij}$  is -1 if the jth Pauli in the domain vector anti-commutes with the ith Pauli in the image.

Therefore, we can get error probabilities from fidelities by using the Walsh-Hadamard transform on the fidelities given by lemma 1:

#### Lemma 2: Error probabilities of repeated channel

Let P be a pseudo-local Pauli. The error probability of P associated with the channel  $\mathcal{E}^x = e^{x\Lambda}$  is given by

$$e_P(x) = x^2 |h_P|^2 + x \sum_j |\ell_{j,P}|^2 + O(x^2 (1 - e_I)^2)$$
 (57)

More mathematical details regarding the transformation form fidelities to effective error rates is contained in [34].

## B IBM Quantum Computing Hardware Architectures

The calculations for this project were run on three different IBM hardware platforms (ibmq\_manila, ibmq\_guadalupe, and ibmq\_montreal). On the 5 qubit ibmq\_manila platform, qubits q0, q1, q2, q3, q4 and q5 are used with q0 as the ancilla and q1-q2 as the two-qubit entangling gate. The ibmq\_guadalupe processor is a 16 qubit platform. On this processor the qubits used are q6, q7, q10, q12, and q13 with q10 as the ancilla and q6-q7 as the two-qubit entangling gate. For the computation done on the 27 qubit ibmq\_montreal platform, qubits q18, q21, q23, q24, and q25 are used with q23 as the ancilla and q18-q21 as the two-qubit entangling gate. The computations on the 5 qubit ibmq\_manila platform, use q0 as the ancilla and q1-q2 as the two-qubit gate. Fig. 8 graphically shows these qubit topologies for each platform. We also ran computations on the Keysight TrueQ simulator [62] for the analysis discussed in the supplemental material in Section 4.2.

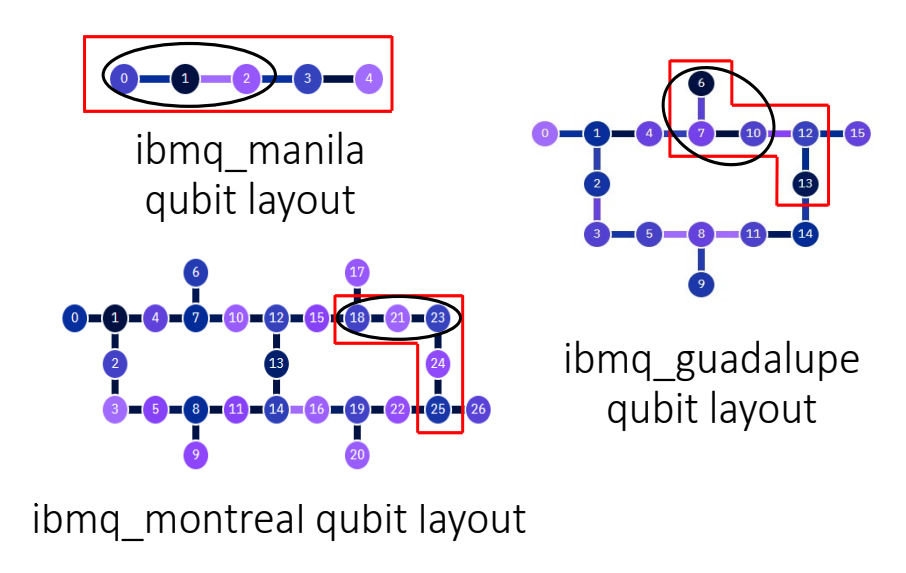


Figure 8: IBM quantum hardware platforms and specific qubits used on each to run the 4 qubit spin-spin correlation function circuit. The black circles indicate the specific qubits used for the KNR two-qubit CNOT and ancilla effective dressed cycles and Pauli fidelity calculations

The key metrics associated with each of the processors that help characterize the processor performance are

- Quantum volume (QV) This value measures the performance of gate-based quantum computers, regardless of their underlying technology.
- Circuit Layer Operations per Second (CLOPS) is a measure of how many layers of a QV circuit a quantum processing unit (QPU) can execute per unit of time. The CLOPS is calculated using three key attributes to measure the performance of near-term quantum computers (quality, speed, and scale) [63].

• The Falcon family of devices are medium-scale circuits. They were deployed by IBM as a test environment for demonstrating performance and scalability improvements over previous generation processors. Specifically the r4 is the first revision to deploy multiplexed readout. Previous designs required an independent signal pathway on the chip, as well as in the dilution refrigerator and control electronics for qubit state readout.

The ibmq\_guadalupe is a 16 qubit Falcon r4p system with a quantum volume of 64 and 2.4K CLOPS. The computations on Guadalupe use qubits 6, 7, 10, 12, 13 with qubit 6 being used as the ancilla qubit. The ibmq\_montreal is a 27 qubit Falcon r4 system with a quantum volume of 128 and 2.0K CLOPS. The computations on Montreal use qubits 18, 21, 23, 24, 25 with qubit 18 being used the ancilla qubit.

# C CER Protocol Measurements and Heatmap Methodology

This project measures the noise on the single qubit (q10 in ibmq\_guadalupe, q23 for ibmq\_montreal and q0 for ibmq\_manila). Although the single qubit gates are set to the identity and should remain so despite the increase in noise from the additional CNOT folded hard cycles implemented through the extended CER mitigation protocol, these heatmaps show that what is measured is not what was expected.

The increase in the measured noise on the single qubit is graphically seen in Fig. 9-Fig. 11). These figures are heatmap error signatures showing the magnitude of error recorded on these qubits. A dark color represents a relatively low value for the error; warmer colors represent a higher value. To the right of each figure is a bar with a color gradation and numbers that set the scale for that heatmap representing the level of the infidelity being measured.

Each of the three figures (Fig. 9 - Fig. 11) shows five sub-figures representing the single qubit error measurements for CNOT hard cycle repetitions 1, 3, 5, 7, and 9 for each of the three IBM hardware platforms. The x-label on the heatmap shows the qubit number being measured and the "I" represents the identity gate that is supposed to be detected on that qubit. The y-axis label of the heatmap shows the X, Y and Z Paulis for that qubit.

Ideally if there were no errors, each of the X, Y and Z Paulis should display a dark color indicating that the difference in the magnitude of the error between what is measured and the identity value that is supposed to be detected on that qubit is minimal. Warmer colors on the heatmap indicate there is an error on that qubit. The magnitude of the error for that Pauli corresponds to the color bar gradation on the scale on the right hand side of each figure.

These heatmaps also clearly show that as the number of hard cycles is increased from 1 to 9, the magnitude of the single qubit Pauli errors (especially the Z error) grows by an order of magnitude on each of the 3 different hardware platforms. This is a graphical signature that the CNOT folded cycles are contributing an increasing

magnitude of error that is detected by the deviation of the single spectator qubit from what should have been an identity gate signature.

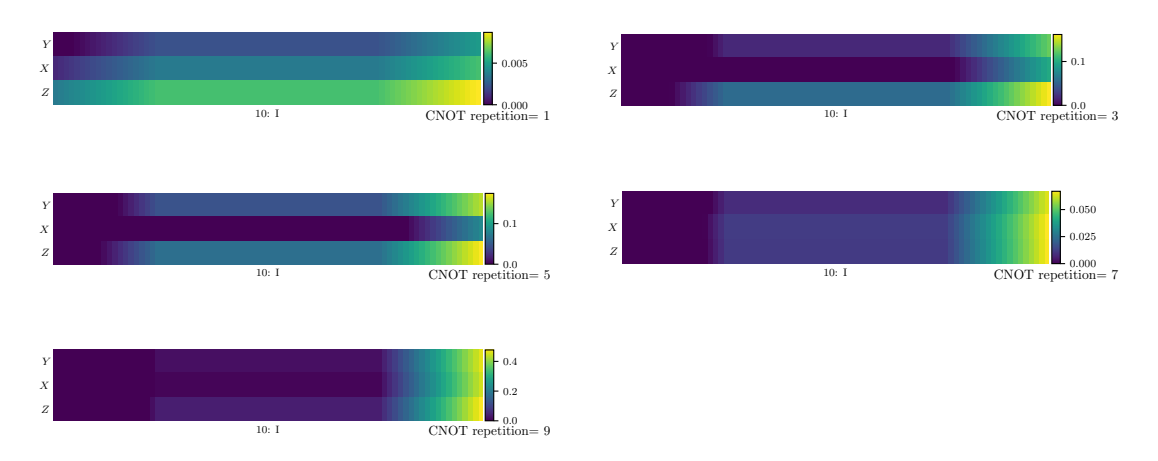


Figure 9: Heatmap of IBM Guadalupe processor

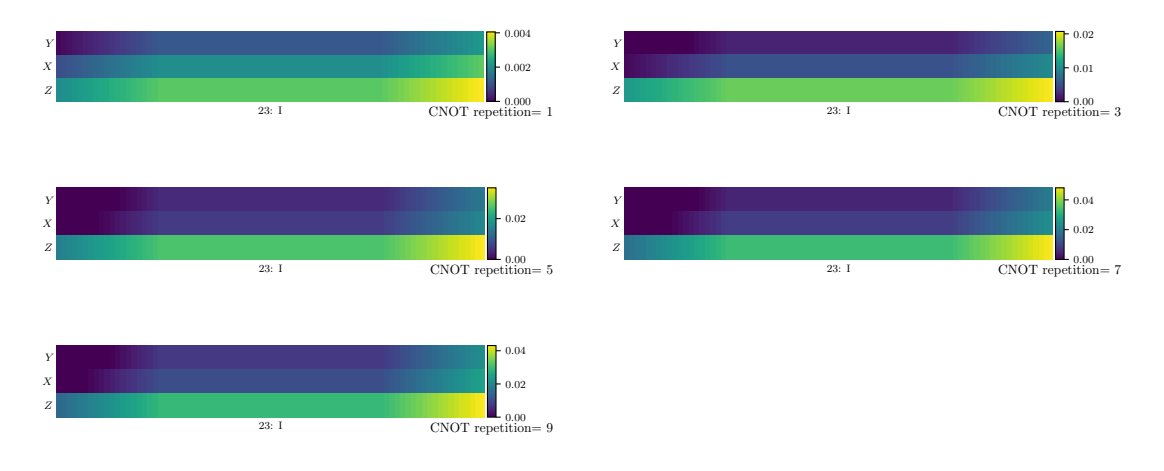


Figure 10: Heatmap of IBM Montreal processor.

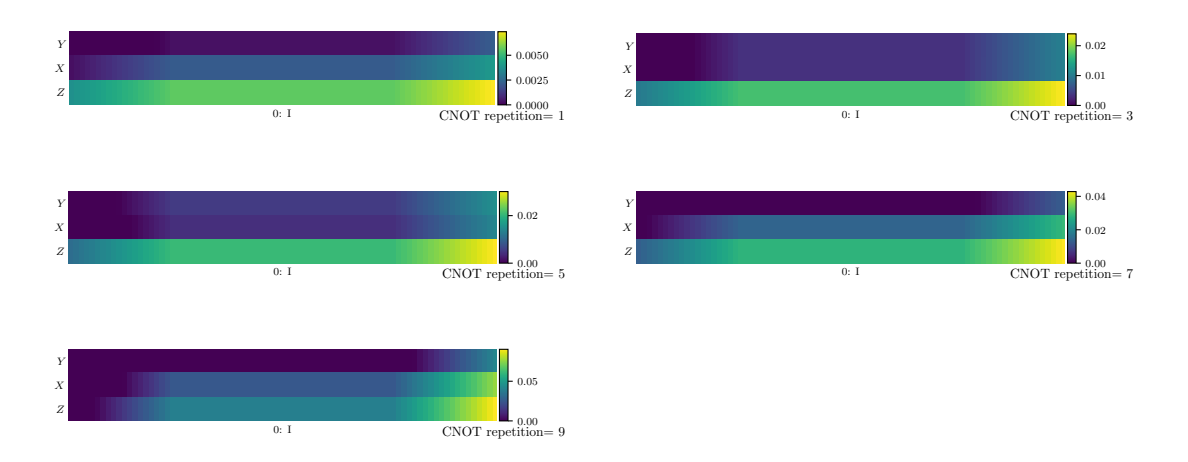


Figure 11: Heatmap of IBM Manila processor